Comparison of ocean heat content from two eddy-resolving hindcast simulations with OFES1 and OFES2

Fanglou Liao[1,2], Xiao Hua Wang[2*] and Zhiqiang Liu[1,3*]

[1]Department of Ocean Science and Engineering, Southern University of Science and Technology, Shenzhen, 518055, China

[2]The Sino-Australian Research Consortium for Coastal Management, School of Science, The University of New South Wales, Canberra, 2610, Australia

[3]Southern Marine Science and Engineering Guangdong Laboratory (Guangzhou), Guangzhou, 511458, China

Correspondence to: Zhiqiang Liu (liuzq@sustech.edu.cn) or Xiao Hua Wang (x.h.wang@unsw.edu.au)

Abstract. The ocean heat content (OHC) estimates from eddy-resolving hindcast simulations from the Ocean General Circulation Model for the Earth Simulator Version 1 (OFES1) and Version 2 (OFES2), and a global objective analysis of subsurface temperature observations (EN4) were compared. OHC increased in most of the global ocean above 2000 m in the EN4 and OFES1 over 1960–2016, mainly a result of deepening of neutral density surfaces, with variations along the neutral density surfaces of regional importance. We found substantial differences in the temporal and spatial distributions of the OHC between the two OFES hindcasts, especially in the Atlantic Ocean. A basin-wide heat budget analysis showed that there was less surface heating for the major basins in the OFES2. The horizontal heat advection was largely similar but the OFES2 had a much stronger meridional heat advection associated with the Indonesian Throughflow (ITF) above 300 m. Also, large discrepancies in the vertical heat advection based on the two OFES data were also identified, especially at the 300 m in the Indian Ocean. Therefore, we concluded that there exist large discrepancies in the inferred vertical heat diffusion (cannot be directly diagnosed in this paper due to data availability), which, along with the different sea surface heat flux and vertical heat advection, were the major factors responsible for the examined OHC differences. This work may be a useful reference for future OFES users.

1 Introduction

The global ocean has stored over 90% of the extra heat added to the Earth system since 1955, causing a significant increase in the ocean heat content (OHC) (Levitus et al., 2012; IPCC 2013). The OHC is therefore an important indicator of climate change, and provides useful bounds in estimating the Earth's energy imbalance (Palmer et al., 2011; Von Schuckmann et al., 2016). Although natural factors such as the El Niño–Southern Oscillation (ENSO) and volcanic eruptions can affect the OHC (Balmaseda et al., 2013; Church et al., 2005), the recent warming has mostly resulted from greenhouse gases accumulating in the atmosphere (Abraham et al., 2013; Gleckler et al., 2012; Pierce et al., 2006).

As a major concern in both the oceanography and climate communities, the OHC has attracted a great deal of attention. Although direct observational records are the most trustworthy data in determining the oceanic thermal state, the fact is that measurements are far from dense enough in both the temporal and spatial domains, especially for the deep and abyssal oceans. This situatione sparseness of observations has greatly improved since the launch of a global

35 array of profiling floats, the Argo, in 2000s. However, the spatial resolution of the Argo program of approximately

36 300 km is not ~~able~~ high enough to capture mesoscale structures (Sasaki et al., 2020, hereafter **S2020**). Several

37 approaches exist to fill the temporal and spatial gaps in global temperature measurements, and can be used to produce

38 gridded temperature fields to estimate the OHC. These approaches include the objective analysis of observational data

39 and ocean reanalysis combing physical ocean models with observations. In addition, ocean general circulation models

40 (OGCMs) provide temperature fields by solving the primitive equations of fluid motion and state. Although OGCMs

41 are dynamically consistent (the resulting fields satisfy the underlying fluid dynamics and thermodynamics equations),

42 some are not constrained by observations. How multi-scale dynamical processes are represented in these

43 unconstrained models and their implementation of external forcing significantly impact their OHC estimates.

44 The Ocean General Circulation Model for the Earth Simulator (OFES; Masumoto et al., 2004; Sasaki et al., 2004),

45 developed by the Japan Agency for Marine-Earth Science and Technology (JAMSTEC) and other institutes, is a well-

46 known eddy-resolving ocean model, and the hindcast simulation of the OFES Version 1 (OFES1) has been widely

47 used (Chen et al., 2013; Dong et al., 2011; Du et al., 2005; Sasaki et al., 2020; Wang et al., 2013). The hindcast

48 simulation based on the OFES Version 2 (OFES2) has now been released, and certain improvements have been

49 demonstrated over the OFES1 (**S2020**). For example, the authors found smaller bias in the global sea surface

50 temperature (SST), sea surface salinity (SSS) and the water mass properties in the Indonesian and Arabian Seas. To

51 our knowledge, however, a comparison of the multi-decadal OHC at a basin or global scale from the OFES1 and

52 OFES2 is lacking. As this high-resolution quasi-global model is expected to be widely used in the oceanography and

53 climate communities for examining the ocean state in the near future, it is necessary to compare the OHC estimates

54 from these two OFES versions as an indicator of the potential improvements in the OFES2 over the OFES1, and also

55 of their adaptability to the OHC-related studies. This is further motivated by the finding that subsurface oceanic fields

56 could be notably different between the results of two OFES runs with different atmospheric forcing, despite their

57 results in the near-surface may be similar (Kutsuwada et al., 2019).

58 The aim of this paper is twofold: (1) to estimate the OHC in the global ocean and each major basin using the OFES1

59 and OFES2, with primary focus on their differences; (2) to understand the causes of the differences between these two

60 simulations. To this end, we used the potential temperature θ to calculate the OHC from 1960 to 2016 for both the

61 global ocean and the major basins, the Pacific Ocean, the Atlantic Ocean and the Indian Ocean, between 64° S and

62 64° N.

63 In Section 2, we give a brief description to the data and methods used here. In Section 3, we describe and discuss

64 the OHC differences between the datasets in both the temporal and spatial domains. A tentative analysis of the possible

65 causes of the differences is also conducted. Sections 4 summarises the principal points and possible extensions

66 involving factors that were not examined here due to data availability but could be important. Future work is therefore

67 expected to improve on our work here.

68

69

2 Data and Methods

2.1 Data

Potential temperature θ from both the OFES1 and OFES2 were used to calculate the global and basin OHCs for comparison with each other and with the OHC calculated from the observation-based EN4. Although results from the EN4 cannot be taken as the actual oceanic state, it has been widely used in OHC-related studies (Allison et al., 2019; Carton et al., 2019; Häkkinen et al., 2016; Trenberth et al., 2016; Wang et al., 2018). A brief description of the three datasets is given below; readers are referred to Sasaki et al. (2004), Sasaki et al. (2020) and Good et al. (2013) for more details.

The OFES1 has a horizontal spatial resolution of 0.1° and 54 vertical levels with a maximum depth of 6065 m (Sasaki et al., 2004); this high lateral resolution enables it to resolve mesoscale processes. Following a 50-year climatological simulation, the hindcast simulation of the OFES1 was integrated from 1950 to two years ago (the publically available data is till 2017). The multi-decadal integration period makes it possible to perform an analysis of oceanic fields at temporal scales from intraseasonal to multi-decadal. Unlike most other datasets used for OHC estimates, the OFES1 is an ocean modelling with no observational constraints. Therefore, it can be used to demonstrate the potential benefits of high resolution and the adaptability of numerical modelling without data assimilation.

The OFES2 has the same horizontal spatial resolution of 0.1°. Vertically, there are 105 levels, with a maximum depth of 7500 m. The OFES1 uses daily National Centers for Environmental Prediction (NCEP) reanalysis (2.5° × 2.5°; Kalnay et al., 1996) for the atmospheric forcing, whereas the OFES2 is forced by the 3-hourly atmospheric surface dataset JRA55-do Version 08 (55km × 55km; Tsujino et al., 2018). Both the temporal and spatial resolutions of the atmospheric forcing have increased greatly in the OFES2. The OFES2 also incorporates river runoff and sea-ice models, although no inclusion of polar areas.

In the horizontal direction, both the OFES1 and OFES2 use a biharmonic mixing scheme to suppress computational noise (**S2020**). The horizontal diffusivity coefficient is equal to -9×10^9 m^4/s at the Equator (**S2020**), and varies proportional to the cube of the cosine of the latitude (personal communication with Hide Sasaki) and. The OFES2 uses a mixed–layer vertical mixing scheme (Noh and Jin Kim 1999) with parametrization of tidal-energy dissipation (Jayne and St. Laurent 2001; St. Laurent et al., 2002), whereas the OFES1 uses the K-profile parameterization (KPP) scheme (Large et al., 1994). With the temperature and salinity on 1st January 1958 from the OFES1 as the initial conditions, the OFES2 used here has been integrated from 1958 to 2016. To reduce the computation and archive cost, we subsampled the OFES1 and OFES2 data every 5 grid points in the horizontal direction.

To evaluate the OHC objectively from the two OFES data, we used the EN4 from the UK Meteorological Office Hadley Centre as a reference. Note that the EN4 version we used is the EN4.2.1, with bias corrected following Levitus et al. (2009). The EN4 data can be considered as an objective analysis that is primarily based on observations (Good et al., 2013), with a horizontal resolution of 1° and 42 vertical levels down to 5350 m. The EN4 assimilates data mainly from the World Ocean Database (WOD) and the Coriolis dataset for ReAnalysis (CORA). Pre–processing and quality checks are conducted before the observational data are used to construct this objective analysis product.

Although we used the EN4 results as a reference for evaluating the OFES performance in simulating the 57-year ocean thermal state, the EN4 cannot be taken as the actual ocean state. The main reason is that the measurements used

107 to construct the EN4 datasets are sparse and inhomogeneous in both the temporal and spatial domains, and far from
108 sufficient to resolve mesoscale or even sub–mesoscale motions. There are more observations in the Northern
109 Hemisphere than in the Southern Hemisphere, and there is also a seasonal bias in the observational data density
110 (Abraham et al. 2013; Smith et al. 2015). A higher density of records became available only after the World Ocean
111 Circulation Experiment (WOCE) in the 1990s and launch of the Argo profiling floats in the 2000s. Table 1 summarizes
112 these three ocean datasets.

113

114 **Table 1.** Description of the OFES1, OFES2 and EN4 datasets. / means not applicable.

	OFES1	OFES2	EN4
Model	MOM3	MOM3	/
Horizontal coverage	75° S – 75° N	76° S – 76° N	83° S – 89° N
Grids	3600 × 1500	3600 × 1520	360 × 173
Maximum depth	6065 m	7500 m	5350 m
Vertical levels	54	105	42
Atmospheric forcing	Daily NCEP/ NCAR reanalysis	3–hourly JRA55–do Ver.08	/
Data assimilated	/	/	WOD, CORA
Time span	1950 – 2017	1958 – 2016	1900 – 2021

115

116   We considered water from the sea surface to around 2000 m and divided it into three layers: upper (0–300 m);
117 middle (300–700 m); and lower (700–2000 m). The ocean above 2000 m has often been divided into two layers, 0–
118 700 m and 700–2000 (or even one: 0–2000 m) (Allison et al., 2019; Hakkinen et al., 2016; Häkkinen et al., 2015;
119 Levitus et al., 2012; Zanna et al., 2019); our analysis here will show that it is in fact necessary to divide it into three
120 layers for our purpose, as did Liang et al. (2021). The temperature and salinity characteristics of the upper ocean,
121 above 300 m, were also analysed in Carton et al. (2018, 2019).
122   The reasons for ignoring water below 2000 m are mainly fourfold. Firstly, the simulated behaviour of the deep
123 ocean depends sensitively on the spin-up of the numerical simulation, which is almost always incomplete (Wunsch
124 2011), at least in the first decade. Secondly, the observational data used in the EN4 are largely confined to the ocean
125 above 2000 m (many available measurements do not even go down this deep (personal communication with the EN4
126 UK Meteorological Office Hadley Centre)), with a much lower density of data in the deep and abyssal oceans. Thirdly,
127 the data in the EN4 version that we used here are bias–corrected, following Levitus et al. (2009), in which only the
128 ocean above 700 m was considered. Therefore, for instance, the Expendable Bathythermograph (XBT) profiles below
129 700 m are corrected using the correction values provided for 700 m (personal communication from the UK
130 Meteorology Office Hadley Centre). Lastly, as can be seen, the maximum depth differs by more than 2000 m between
131 the OFES2 and EN4. It was felt that a full-depth OHC is not highly comparable between the three datasets. This,
132 however, does not imply that the deep ocean can be ignored; it can play an essential role in regulating the global-ocean
133 thermal state (Desbruyeres et al. 2016; Desbruyères et al. 2017; Palmer et al. 2011). It is expected that a much better
134 understanding of the deep and abyssal ocean state will be gained with the implementation of the Deep Argo program,
135 partially validated by Johnson et al. (2019).

136   **2.2 Methods**

137   We compared the three datasets over the period 1960–2016. The OHC values here are the OHC anomalies relative to

138   estimates in 1960. At each grid point, the OHC is given by

139    $$\text{OHC} = \rho \delta v C_p (\theta - \theta_{1960}) = \rho \delta v C_p \Delta \theta, \qquad (1)$$

140   where ρ is the seawater density (kg/m^3), δv the grid volume (m^3), C_p the specific heat of seawater at constant pressure

141   (J/kg/°C), θ the yearly potential temperature (°C) and θ_{1960} the averaged potential temperature in 1960. The total

142   OHC in the upper ocean layer (above 300 m) is the integral of Eq. (1) from 0 to 300 m. Similar procedures apply to

143   the other two layers. A value of 4.1×10^6 kg.J/m^3/°C was used for the product of ρ and specific heat of seawater C_p

144   (Palmer et al., 2011).

145   Both the global and individual-basin OHCs were calculated for comparison. Fig. 1 shows the domains of the Pacific,

146   Atlantic and Indian Oceans between 64° S and 64° N, with their respective marginal seas included. The definition of

147   the marginal seas of the Pacific and Indian Oceans may be inconsistent with some other studies. The major water

148   passages connecting the different basins are also labelled in Fig. 1a. A schematic diagram shows the primary processes

149   determining the OHC of an ocean basin (Fig. 1b).

150
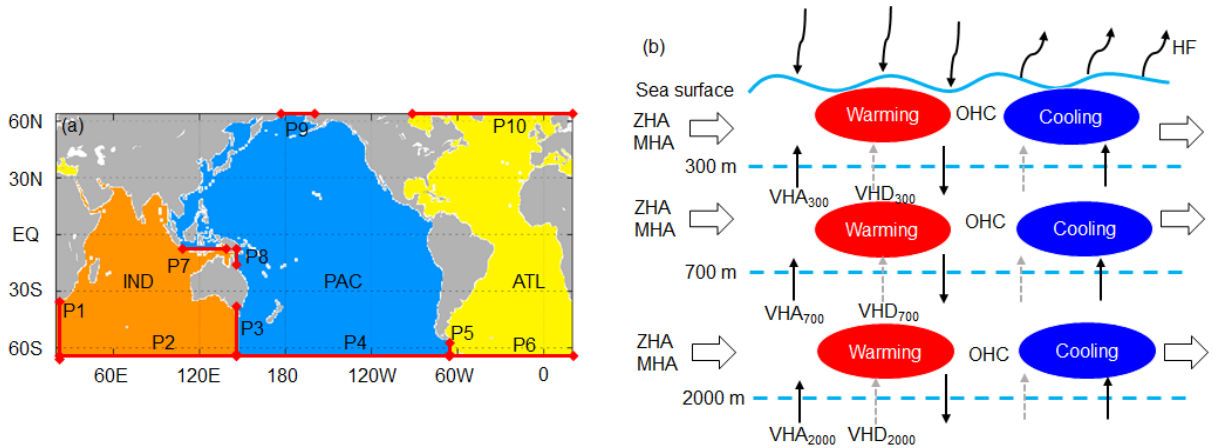
151

152   **Figure 1.** Domains of the major basins between 64° S and 64° N and a schematic diagram of the primary processes controlling the
153   thermal state of an ocean. (**a**) The PAC stands for the Pacific Ocean, the ATL for the Atlantic Ocean and the IND for the Indian
154   Ocean. The basin domain is extracted using the gcmfaces package (Forget et al., 2015) and then interpolated to the corresponding
155   grid of each product. Grey indicates the land. The red solid lines with diamond arrow stand for the water passages connecting
156   different basins. We label it with the capital letter P (abbreviation for passage) and a serial number. EQ stands for the Equator. (**b**)
157   We use a light blue curve to represent the ~~wave-shaped~~free sea surface and three dashed lines to indicate the 300 m, 700 m and
158   2000 m depth. The curve arrow represents the net heat flux (HF) through the ocean surface. The black hollow arrows show the
159   zonal (ZHA) or meridional (MHA) heat advection. The black thin arrow represents the vertical heat advection (VHA) and the grey
160   dash arrow stands for the vertical heat diffusion (VHD). The red ellipse illustrates warming water and the blue ellipse cooling water.
161   P1: (20° E, 64° S – 34.5° S); P2: (20° E – 146.5° E, 64° S); P3: (147° E, 64° S – 36.5° S); P4: (147° E – 65.5° W, 64° S); P5: (67°
162   W, 64° S –55° S); P6: (65° W – 19.5° E, 64° S); P7: (118.5° E – 138.5° E, 8.5° S); P8: (142° E, 12.5° S – 8° S); P9: (172.5° W –
163   166.5° W, 64.~~5~~ N); P10: (88° W – ~~24~~19.5° E, 64.~~5~~ N).

164

165   In addition, the $\Delta \theta$ at a fixed depth are decomposed into a heave (HV component (second term in Eq. (2) below)

166   and a spice (SP) component (third term in Eq. (2)) (Bindoff and McDougall 1994). The HV-related warming or cooling

167   is a result of vertical displacement of the neutral density surfaces (a continuous analogue of discretely referenced

168   potential density surfaces; Jackett and McDougall, 1997). In general, both the dynamical changes and the change in

169   the renewal rates of water masses can induce vertical displacement and thus the HV-related warming or cooling as a

170   consequence (Bindoff and McDougall, 1994). The SP represents warming or cooling as a result of density

171   compensation in the θ and salinity (S) along the neutral density surfaces. This decomposition of $\Delta\theta$ helps to better

172   understand the contributions and ways of different water masses in accounting for the OHC. The formula decomposing

173   the potential temperature is

$$d\theta/dt\,|z = -\,\overset{HV}{\overbrace{dz/dt|n\,d\theta/dz}} + \overset{SP}{\overbrace{d\theta/dt|n}} \tag{2}$$

175   where t is the time (year), z means the depth (m) and $|n$ means along the neutral density surface.

176   A program by Jackett and McDougall (1997) was used to calculate the neutral densities, HV and SP, . this This

177   code is based on the UNESCO (The United Nations Educational, Scientific and Cultural Organization) 1983 for the

178   computation   of   fundamental   properties   of   seawater   (http://www.teos–

179   10.org/preteos10_software/neutral_density.html); we used its Matlab version. The main inputs for this program are

180   the θ and S. As the code limits the latitude to between 80° S and 64° N, we further confine our investigation domain

181   to be 64° from the equator; this also avoids comparisons in sea-ice impacted areas, knowing that only the OFES2

182   includes a sea-ice model.

183   To analyze the causes of OHC differences from thermodynamic and dynamic perspectives, we calculated the

184   surface heat flux (HF), zonal heat advection (ZHA), meridional heat advection (MHA) and vertical heat advection

185   (VHA). Owing to a temporary suspension of the OFES2 data by the JAMSTEC, we could not access the vertical

186   diffusivity data of the OFES2 (OFES1 does not provide these data) when preparing this manuscript. This prevents us

187   to directly comparing the vertical diffusion of heat from the OFES1 and OFES2. Alternatively, we calculated the

188   residual of the total OHC and all the other heat inputs (HF, ZHA, MHA and VHA), and took this as a proxy for the

189   vertical diffusion. As the horizontal heat diffusion was found to be much weaker than the ZHA and MHA (not shown),

190   we did not include it in the analysis. A diagram of the primary processes is shown in Fig. 1b. Note that the linear trend

191   in the following sections was calculated using the multiple linear regression using least squares, and we used the 95%

192   confidence level.

3 Results

194   The principal aim here is to compare the results from the OFES1 and OFES2, with the EN4 acting as an observation-

195   based reference. If there was a significant difference between the OFES2 result and that of one or both of the other

196   two datasets, does this represent a real phenomenon not present in the other two widely used datasets or is it an

197   unwanted property of the newly released OFES2 simulation? In this section, we compare the three sets of results for

198   the global ocean, and for each of the Pacific, Atlantic and Indian Oceans individually.

3.1 Time evolution of the OHC, HV and SP from 1960 to 2016

3.1.1 The time series of OHC, HV and SP

Figs. 2–4 present the time series of the total OHC, and its HV and SP components for the upper (0–300 m), middle (300–700 m) and lower (700–2000 m) ocean layer, respectively. Note that OHC, HV and SP were calculated as the anomaly relative to the estimates in 1960, and converted to an equivalent heat flux applying over the entire surface area of the Earth, as suggested by one reviewer.

Upper layer

For the global ocean between 0–300 m, all three data indicate cooling from around 1963 to 1966 (Fig. 2a), explained as the result of the volcanic eruption of Mount Agung (Balmaseda et al. 2013). A similar cooling over this period can also be seen in Domingues et al. (2008) and Allison et al. (2019) for the upper 700 m (their Fig. 1) and Achutarao et al. (2007) for both the 0–700 m and 0–3000 m (their Fig. 1). This short but sharp cooling was found to mainly impact the Pacific Ocean (Fig. 2b). Marked OHC reductions associated with the strong volcanic eruptions of El Chichón in 1982 (a strong ENSO also emerged in 1982–83) and Pinatubo in 1991 were also consistently captured by all the three data.
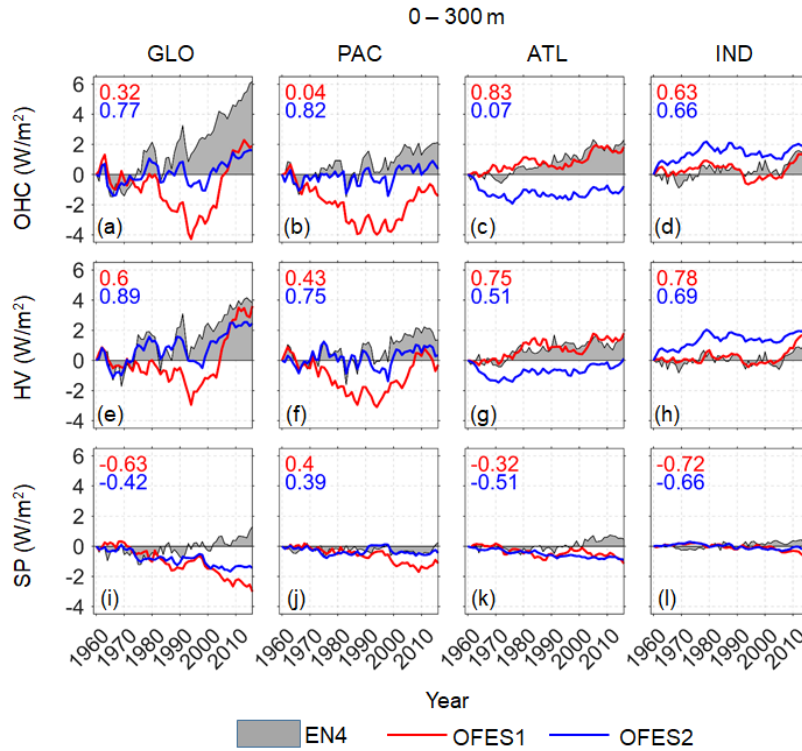
Figure 2. Time series of the global and basin–wide OHC (**top**), HV (**middle**) and SP (**bottom**) between 0–300 m based on the three temperature products. The OHC, HV and SP here are converted to the accumulative heating in W m^{-2} applied over the entire surface of Earth. Grey shadow: EN4; red solid line: OFES1; blue solid line: OFES2. Numbers on the left top corners are the correlation coefficients between the OFES1 (red) or OFES2 (blue) and EN4. The OHC hereafter is directly calculated from the potential temperature, rather than the sum of the HV and SP.

221   Both the EN4 and OFES2, but not the OFES1, showed a slowdown in warming and even cooling in the Pacific
222   Ocean during the 2000s. This slowdown in Pacific warming corresponded to a sharp warming in the upper layer of
223   the Indian Ocean. This relevance between the Pacific and Indian Ocean was found to be a consequence of an
224   intensifying Indonesian Throughflow, leading to an increased heat transport from the Pacific to the Indian Oceans
225   (Lee et al. 2015; Zhang et al. 2018); however, these two references considered the top 700 m. As will be shown,
226   however, this sudden warming of the Indian Ocean was largely confined to the above 300 m, especially as indicated
227   by the OFES1 and OFES2 (Fig. 3d). The EN4 showed a clear warming acceleration around 2003 in the global ocean
228   above 300 m, which was probably an artefact of the transition of the ocean observation network from a ship-based
229   system to Argo floats (Cheng and Zhu, 2014), although these authors mainly used subsurface temperature data from
230   the World Ocean Database 2009 (WOD09). Interestingly, a dramatic shift can also be seen in the OFES1(Fig. 2a),
231   remembering that the OFES1 is not directly constrained by observations. A major difference in this jump between the
232   EN4 and OFES1 is that it was found to be more closely associated with the SP in the EN4 (Fig. 2i) but with the HV
233   in the OFES1 (Fig. 2e). This spiciness warming around 2003, derived from objective analysis of observational data
234   can serve as a complement of the work by Cheng and Zhu (2014).

235   However, many significant differences can be found between the three datasets. The EN4 indicated an
236   approximately linear warming since around 1970 (Fig. 2a), modulated by the abovementioned climate signals. The
237   OFES1, however, showed that the cooling persisted almost until the beginning of the 1990s, when a similar linear but
238   stronger warming appeared afterwards (Fig. 2a); this is more than 20 years later than that indicated by the EN4. The
239   approximately linear warming appeared even later in the OFES2 from around 2000, and was the weakest among the
240   three datasets.

241   Compared to the OFES1, the OFES2 agreed better with the EN4 in the temporal profile of the global ocean (Fig.
242   2a), which, to some extent, is consistent with the smaller sea surface temperature (SST) bias from the OFES2 than
243   that from the OFES1 when comparing to the World Ocean Atlas 2013 (WOA13) (**S2020**). However, there was a large
244   magnitude difference after 1980. This came mainly from the spiciness component (Fig. 2i), with both the OFES1 and
245   OFES2 indicating clear SP cooling. This may imply some discrepancies in the salinity characteristics from these three
246   data. In contrast, there was quite good agreement in the HV from the EN4 and OFES2 (Fig. 2e).

247   Clear differences can also be easily discerned for each individual basin. The OFES1 differed significantly from the
248   other two in the Pacific Ocean between around 1970–1990, with the other two similar to each other in both the HV
249   and SP. In the Atlantic Ocean, however, the OFES1 agreed with the EN4 quite well in the HV. Although the two
250   OFES datasets had similar spiciness in the Atlantic Ocean, they both disagreed with the spiciness from the EN4. The
251   HV indicated by the OFES2 showed poor agreement with both the EN4 and OFES1 in the 1960s (Fig. 2g). In the
252   Indian Ocean, the OFES1 was much closer to the EN4 than the OFES2. Both the similarities and differences in the
253   OHC came largely from the HV, which dominates the variation of OHC. The notable deviations of the OFES2 relative
254   to others mainly come from the uniquely strong warming in the OFES2 Indian Ocean before around1980 (Fig. 2d).

255   A potential issue of the OFES2 is the spin-up, although it started from the calculated the temperature and salinity
256   fields. Without a knowledge about when it is fully spun-up, we here show and compare its simulated results starting
257   from 1960, only excluding the first two years (1958–1959). It seems that the OFES2 has a good agreement with the

8

258 EN4 since around 1970s in both the Atlantic and Indian Oceans (Fig. 2c, d), which is likely to be related to the better

259 spun-up with time. However, in the Pacific Ocean, the OFES2 was quite similar to the EN4 before 1990, especially

260 in the HV component. This to some extent, may weaken the spin-up argument.

261

262 *Middle layer*

263 In the middle ocean layer (300–700 m) (Fig. 3), there were remarkable differences in the OHC and its HV and SP

264 components between the OFES2 and the other two datasets, most noticeable for the global ocean and the Atlantic

265 Ocean, less so for the Pacific Ocean; there was little difference for the Indian Ocean. The OFES2 showed a moderate

266 Pacific cooling for almost the whole 57–year period and a strong Atlantic cooling trend until around 2000, with a

267 subsequent hiatus in the Atlantic Ocean. There was a minor Indian cooling from the OFES2 in the 1960–70s. In the

268 OFES2, this cooling was mainly due to the decreasing HV, as its spiciness was largely more positive than the other

269 two.
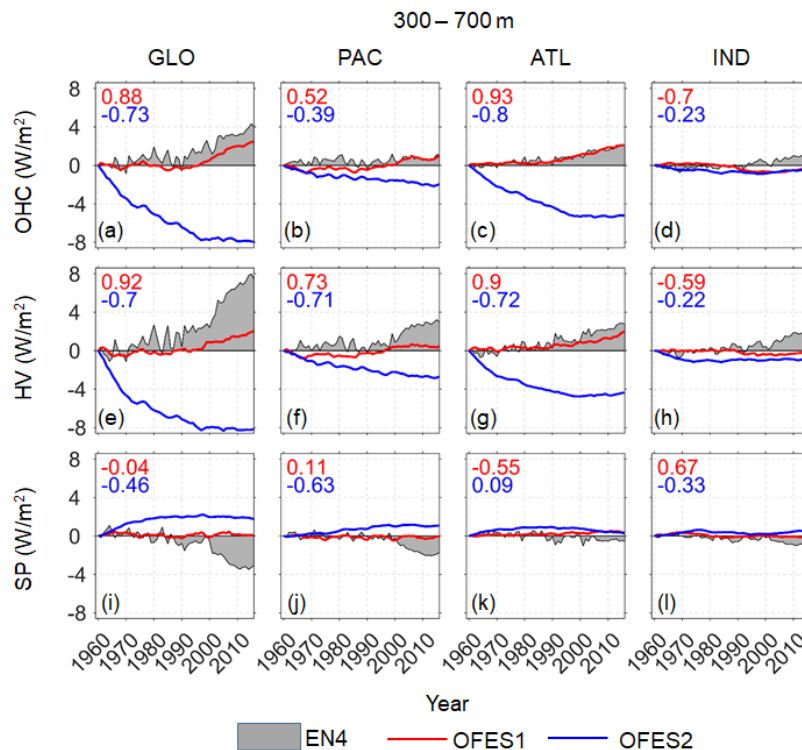
270

271 **Figure 3.** As for Fig.2 but for the middle layer (300–700 m).

272

273   In contrast, both the EN4 and OFES1 indicated that this layer was relatively stable before about 1990. Then, the

274 EN4 and the OFES1 both showed the global ocean and the Atlantic Ocean warming (Fig. 3a, c), mostly due to an

275 increase in the HV (Fig. 3e, g). Despite this good agreement between the EN4 and OFES1, there were notable

276 differences in their HV and SP components. Compared to the OFES1, there was a generally stronger positive HV in

277 the EN4 (Fig. 3e–h), and a stronger but negative SP in the EN4, particularly after about 2000 (Fig. 3i, j). A possible

278 reason for this is the fact that there have been much more observations available since the WOCE (World Ocean

279 Circulation Experiment) in the late 1990s and from Argo since the beginning of 2000s. This may have led to a

280   systematic trend in the observational–based dataset EN4. Unlike in the EN4 and OFES2, the SP variations in the

281   OFES1 were almost invisible for almost all the basins. In addition, aforementioned significant warming acceleration

282   from the early 2000s to 2010s in the Indian Ocean (Fig. 2d) can still be seen in the EN4 (Fig. 3d), but this was almost

283   invisible in the two OFES datasets.

284   One major cause of the profound differences between the OFES2 and the EN4 is the spin-up issue. Indeed, even

285   after 2000, clear differences remain in the global ocean. This, on the one hand, is expected because the middle layer

286   takes more time to be well spun-up compared to the upper layer; on the other hand, suggests that special caution is

287   needed when investigating the multi-decadal variations, or even decadal variations in the recent two decades based on

288   the OFES2.

289
290   *Lower layer*

291   In the lower ocean layer (700–2000 m) (Fig. 4), the OFES2 was clearly again the outlier of the three datasets. It showed

292   that the Atlantic and Indian Oceans experienced cooling from 1960 to the end of 1990s (Fig. 4c, d), then a slight

293   warming. The Pacific Ocean, however, was shown cooling over the whole 57-year period (Fig. 4b). The better

294   agreement with the EN4 since the end of 1990s may be related to the spin-up issue of the OFES2, at least to some

295   extent. However, the agreement between the EN4 and OFES2 was even better than in the middle layer (300–700 m),

296   particularly in the Atlantic and Indian Oceans. This may weaken the spin–up argument, as it is expected that the

297   middle layer was more easily spun–up than the lower layer.

298   The OHC variations from the OFES1 and the EN4 were much the same for the global ocean, but this was a result

299   of the cancelling of the substantial differences in the Pacific and Atlantic Oceans (Fig. 4b, c), and in the HV and SP

300   (Fig. 4e–l). Specifically, there was a larger OHC increase in the Pacific Ocean from the OFES1 than the EN4, but the

301   latter showed a larger OHC increase in the Atlantic Ocean. From the perspective of potential temperature

302   decomposition, the EN4 generally showed a stronger HV increase than the OFES1 in the Atlantic and Indian Oceans

303   (Fig. 4g, h) but a stronger negative SP or weaker positive SP increase (Fig. 4i–l).
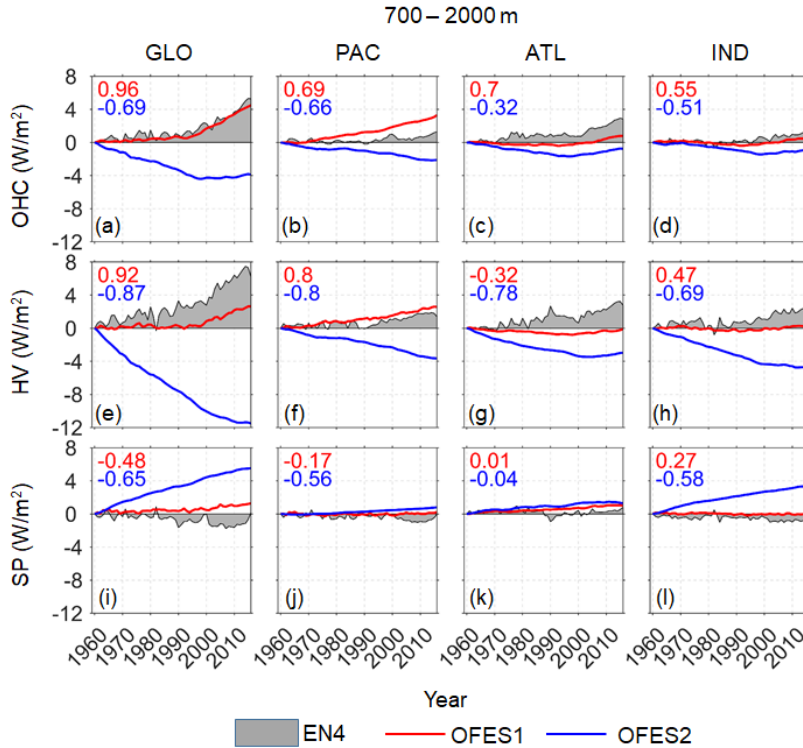
700 – 2000 m

Figure 4. As for Fig.2 but for the lower layer (700–2000 m).

3.1.2 Temporal evolution in the OHC, HV and SP trend

Figs. 2–4 show clearly the similarities and differences between the three datasets in the time series of the OHC, HV and SP for the period 1960–2016; these vary with time. Therefore, in this section, we calculate the linear trend in the OHC, HV and SP over a rolling window of 10 years for the three datasets, following Smith et al. (2015); the results for the three layers are shown in Figs. 5–7, respectively. This helps to quantitatively compare the performance of these data over each temporal window.

Upper layer

The datasets were similar in the profile of the OHC 10-year rolling trend; they captured most of the peaks and troughs. There was better agreement in the Indian Ocean (Fig. 5d) than in the other two basins (Fig. 5b, c) but there were still significant differences even in this shallow layer. The rolling trend for the global ocean from the EN4 was positive most of the time, except at the beginning of the 1960s and at the ends of the 1970s and 1980s (Fig. 5a). However, the OFES1 showed a cooling trend in the global ocean before around 1990; it then indicated a larger warming trend than the other two. The OFES2 generally had a better agreement with the EN4 for the global ocean, but the warming trend was much smaller than that from the EN4 from the late 1960s to around 1990. Since the beginning of 1990s, the trend disparity between the OFES2 and the EN4 was much reduced but the OFES2 still showed a consistently weaker warming trend. This better agreement may be attributed to two causes. Firstly, after around 30-years running, the OFES2 was believed to have been better spun-up and therefore closer to the actual state. Secondly, it is also possible

11

324 that the accuracy of the EN4 data increased as more observational data were included, given that the number of

325 oceanographic observations has increased significantly since the 1990s (e.g. satellite-based SST measurements).

326   Among the differences between the three datasets, the three extreme trend peaks at around 1970, 1980 and 2000

327 (Fig. 5a) are particularly prominent, with remarkable differences between the two OFES and EN4, indicating some

328 deficiencies of numerical modelling in the reproducing of strong climate events. Apart from some minor magnitude

329 differences, the three data agreed best in the Indian Ocean (Fig. 5d). The OFES1 was close to the EN4 in showing

330 significant warming in the Indian Ocean in the 2000s, whereas the OFES2 showed a relatively weaker warming. A

331 second better agreement between the three datasets was reached in the Atlantic Ocean.

332   The HV clearly dominated the 10-year rolling trend in all basins (Fig. 5e–h), and the major differences between

333 the three datasets resulted from differences in the HV component. In addition, there was an apparent out-of-phase

334 relationship between the HV and SP trends in the global ocean and Pacific Ocean. This correspondence between the

335 HV and SP is expected for typical stratification associated with subtropical gyres (Hakkinen et al. 2016), with warm

336 and salty water over the cold and fresh water. The OFES1 and OFES2 were quite close in the simulation of spiciness,

337 particularly in the individual basins (Fig. 5i–l).

338
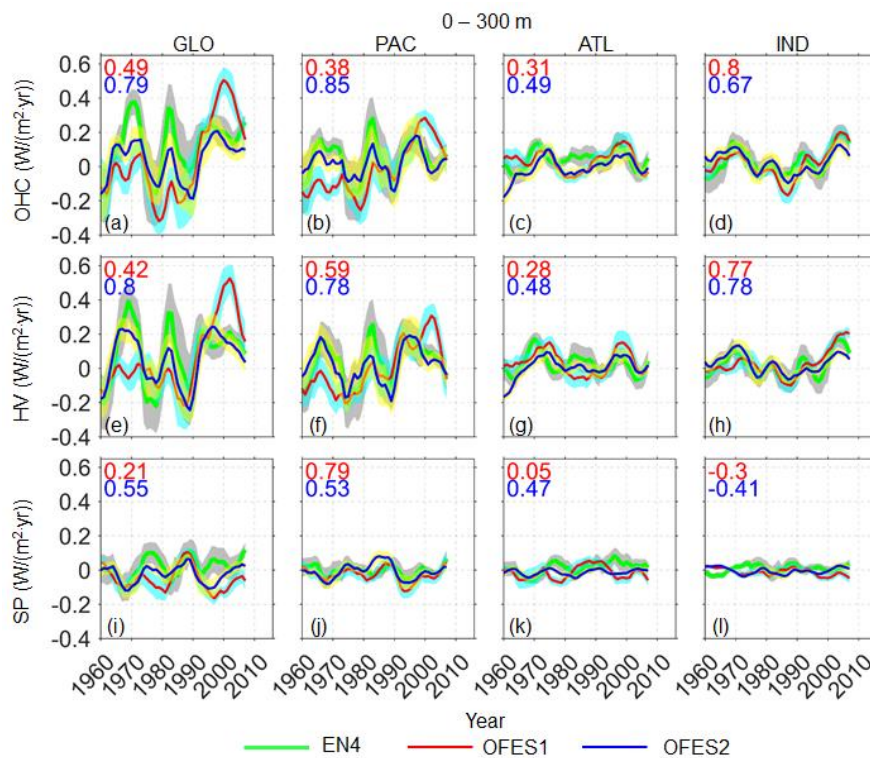
339 **Figure 5.** Temporal evolution of the 10-year rolling trends in the global and basin OHCs (**top row**), HV (**middle row**) and SP
340 (**bottom row**) in the top ocean layer (0–300 m), based on the three datasets. Numbers in the top left corners are the correlation
341 coefficients between the EN4 and the OFES1 (red) or OFES2 (blue). The OHC, HV and SP were converted to accumulative heating
342 (~~W~~ W/m^{-2}) over the entire surface of the Earth. Thick green line: EN4 (grey shadow: 95% confidence interval); thin red solid line:
343 OFES1 (cyan shadow: 95% confidence interval); thin blue solid line: OFES2 (yellow shadow: 95% confidence interval). ~~The OHC~~
344 ~~from now on is calculated directly from the potential temperature, rather than as the sum of the HV and SP.~~

345

346 *Middle layer*

347 The variation in the 10-year rolling trend from the OFES1 and the EN4 was much the same for the global, Pacific and

348 Atlantic Oceans, but the latter dataset having a much large uncertainty (Fig. 6). The OFES2 showed significantly

349 different and generally cooling trend, especially concentrated in the Atlantic Ocean, consistent with Fig. 3; the reasons

350 why notable cooling trend from the OFES2 in the Atlantic Ocean weakened with time needs a further detailed study.

351 It was found that the cooling trend in the OHC from the OFES2 came largely from the HV. In the Pacific Ocean (Fig.

352 6b), the OFES2 consistently show a weak cooling trend, but in the middle and late 1960s and after around 1980, both

353 the EN4 and OFES1 showed a warming trend of similar magnitudes. The OFES1 also agreed well with the EN4 in

354 the Atlantic Ocean, both indicating weak warming for most of the period but also sporadic cooling trend. However,

355 these good agreements are the compensation results of the significantly different HV and SP components from the

356 OFES1 and EN4. For example, the EN4 showed much stronger HV warming trend than the OFES1 in the Pacific

357 Ocean since the early 1990s, but in the meantime, the EN4 also indicated strong SP cooling trend. In the Indian Ocean,

358 the EN4 presented warming trend over much of the 57-year period, whereas the two OFES datasets showed weak

359 variations and reversals between warming and cooling.
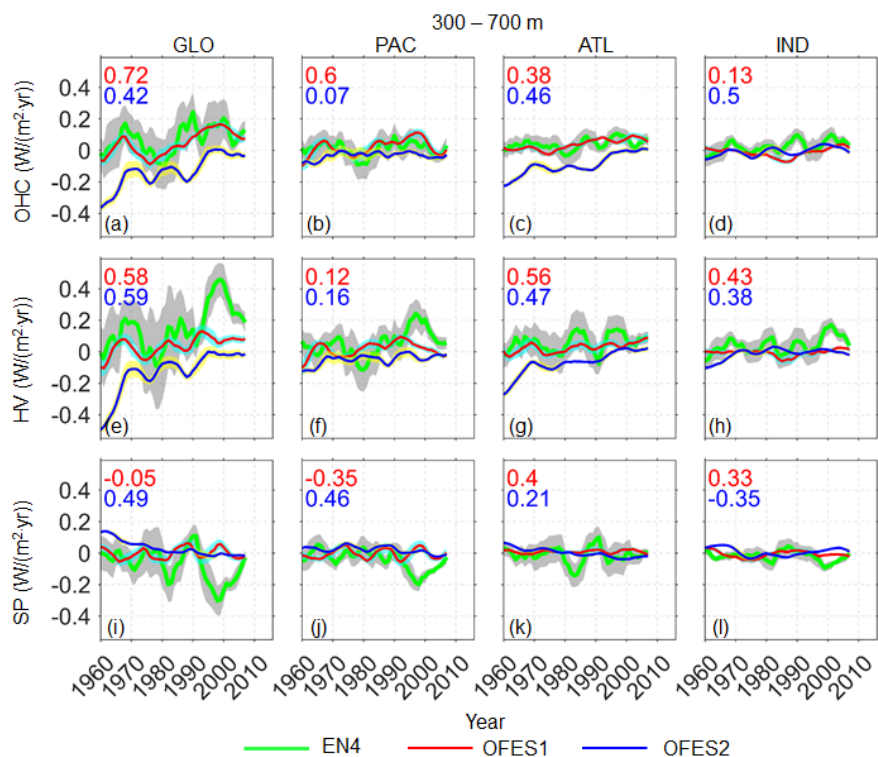

360

361 **Figure 6.** As for Fig. 5 but for middle layer (300–700 m).

362

363 *Lower layer*

364 As in the middle layer, the OFES2 differed significantly from other two datasets by showing a cooling trend in the

365 global ocean until about 2000 (Fig. 7a). Although a warming trend appeared in the global ocean in the OFES2, the

366 intensity was much lower than that of the EN4 and OFES1. The major differences between the two OFES datasets

367 occurred in the Pacific Ocean (Fig. 7b), and was mostly HV-associated. Despite of the good agreements in the OHC

368 trend between the OFES1 and OFES2 in the Atlantic and Indian Oceans (Fig. 7c, d), their HV and SP components

13

369 were markedly different, especially in the Indian Ocean (Fig. 7h, l). The OFES1 and the EN4 showed much the same

370 global OHC trend (Fig. 7a), but again this was the result of the significant HV and SP components cancelling each

371 other. ~~The excellent agreement between the EN4 and OFES1 in each basin (Fig. 7b–d) was also the result of~~

372 ~~cancellations of notable basin-wide differences, especially in the Pacific and Atlantic Oceans (Fig. 7b, c).~~

373   To summarize, the OFES2 showed some improvement (better agreement with the EN4) over the OFES1 in the

374 upper layer (above 300 m), but was more of an outlier in the other two layers. It is essential to examine the HV and

375 SP when investigating the OHC trends, as different data products may show much the same OHC evolution, but

376 substantially different HV and SP.
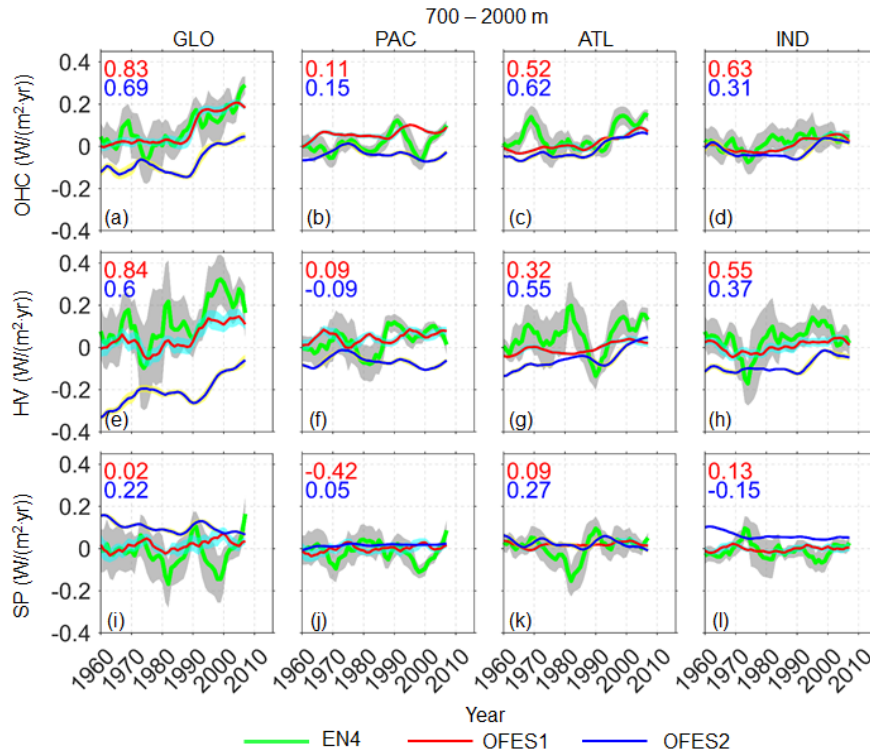
377

378 **Figure 7.** As for Fig. 6 but for the lower layer (700–2000 m).

379 **3.2 Temporal evolution of the zonal-averaged potential temperature trend**

380 Section 3.1 focused on the temporal characteristics of the global and basin-wide OHC, HV and SP from the three

381 datasets. Although both similarities and differences were demonstrated, this comparison only in the temporal

382 domain lacked spatial information. Here, we aim at understanding how the differences were distributed in the

383 meridional direction. As a first step, we calculated the 10-year rolling trends in the zonal-averaged potential

384 temperature change for all three datasets (Figs. 8–10). We also calculated the HV and SP components

385 (Supplementary Information, Figs. 1–6).

386   The complex patterns shown in Figs. 8–10 defy easy interpretation, so we focus on the large-scale patterns of the

387 similarities and differences.

388

389 *Upper layer*

14

390 There was a generally reasonable correlation between these datasets at latitudes 30–60° N for both the Pacific and
391 Atlantic Oceans (there is no northern high latitude in the Indian Ocean). More specifically, there was a wave-like
392 cooling trend propagating from around 60° N to 30° N from 1960 to the end of the 1970s in the global ocean; this
393 apparent propagation was especially clear in the EN4 and OFES2. In addition, there was northward propagation of a
394 cooling trend in the 1990s between around 30–45° N. It is reasonable to attribute this cooling to the volcanic
395 eruption of Indonesia's Mount Agung in 1963, Mexico's El Chichón in 1982 and the Philippines' Mount Pinatubo in
396 1991; the two hindcast simulations were able to reproduce these climate events.

397 Following these cooling events, there were three subsequent warming trends, as the ocean surface temperature
398 returned back to normal once the aerosols released over several years of volcanic eruptions finally dispersed. Of
399 these warming trends, that following the El Chichón eruption was the most significant; there was a clear northward
400 propagation of the warming from around 30° N to the subpolar areas. Interestingly, the contributions to this large-
401 scale warming and cooling by the SP was comparably to the HV (Supplementary Information, Figs. S1–2),
402 contradicting the general sense that the HV dominates the potential temperature change. In fact, the above-
403 mentioned propagation of the cooling patch from around 60 to 30° N in the 1960–70s was, to a lager extent,
404 associated with the SP.
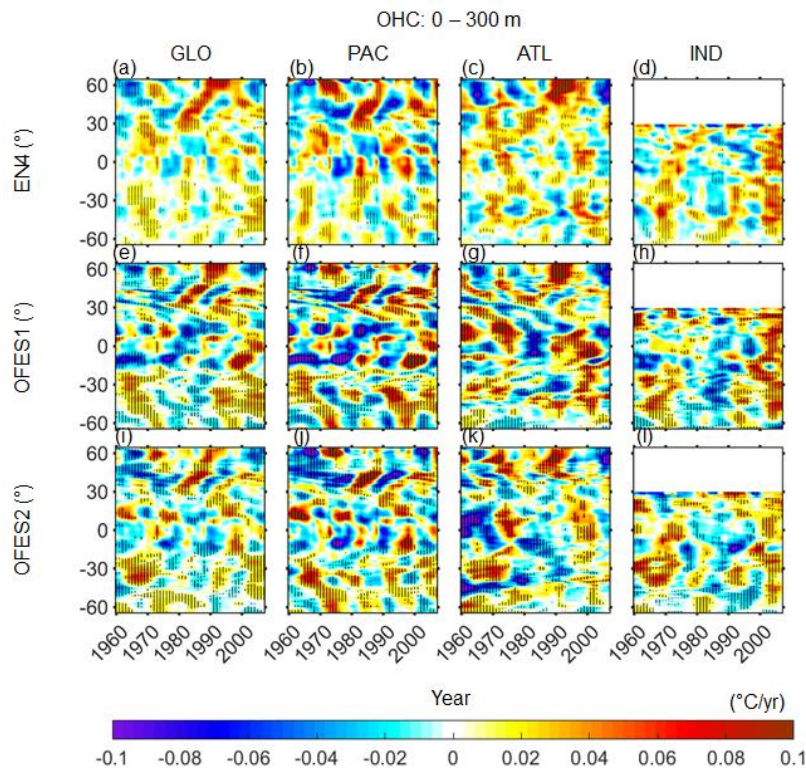
405
406 **Figure 8.** Temporal evolution of 10-year rolling trend of the zonal averaged potential temperature change in the upper layer of
407 the ocean (0–300 m). **Left to right:** global, Pacific, Atlantic and Indian Ocean. **Top to bottom:** EN4, OFES1 and OFES2.
408 Horizontal axis: year; vertical axis: latitude. Stippling indicates the 95% confidence level. The HV and SP counterparts are in the
409 Supplementary Information, Figs. S1–6.
410

411 Equatorward of 30°, large differences emerged in the data. Strong cooling was particularly visible in the OFES1
412 in the Pacific tropics before around 1990 (Fig. 8f), corresponding to the persistent cooling in the global ocean and

413   Pacific Ocean from the OFEES1 in Fig. 2. In the OFES2 Pacific Ocean, clear differences from the EN4 were discerned

414   in the low latitudes before around 1980, then a similar pattern to the EN4 was simulated by the OFES2. In the Atlantic

415   tropics (Fig. 8, 3rd column), there was moderate-to-intense warming in the 1960s in the EN4 and OFES1, but

416   considerable cooling in the OFES2, which may be a result of poor spun-up in the OFES2. All three datasets captured

417   the Atlantic tropical warming in the 1970s, and from the 1990s to the 2000s, but the two OFES datasets estimating a

418   much stronger intensity than the EN4, especially the OFES1. In addition, the OFES1 showed a significant cooling

419   appearing in the Atlantic tropics in the 1980s (Fig. 8g). Although a similar contemporary cooling was shown by the

420   OFES2, its cooling center was shifted several degrees southward. This 1980s Atlantic tropical cooling was

421   comparatively weak in the EN4. Moreover, the OFES2 indicated an approximate 20-year cooling in the vicinity of

422   45°S in the Atlantic Ocean (Fig. 8k); this cooling in the 1960s existed, but weaker in intensity, in the EN4 and OFES1.

423   In the Indian Ocean, the most significant agreement among the three datasets was the intense warming in the 2000s.

424   In addition, there were some common cooling patterns from the 1980s to the 1990s in all three datasets. Over these

425   latitudes, the HV accounted for more of the potential temperature change than the SP, with the latter in general

426   counteracting the HV (Supplementary Information, Figs. S1–2).

427   A general property of the similarities and differences between these three datasets is that a better agreement was

428   reached in the poleward of 30° than the latitudes equatorward of 30°. A possible explanation for this latitudinal

429   dependence is that a deeper thermocline at a higher latitudes responded less sensitively to the applied wind stress

430   (Kutsuwada et al., 2019). Kutsuwada et al. (2019) found that the NCEP reanalysis wind stress used as the atmospheric

431   forcing of the OFES1 had some issues, causing much shallower thermocline in the tropical North Pacific Ocean and

432   therefore large negative temperature differences when comparing to the observations and an OFES version forced by

433   the wind stress from the satellite measurements (QSCAT). The authors also claimed that the JRA 55 wind stress had

434   similar problems with the NCEP wind. Indeed, the intense Pacific cooling patches in Fig. 2f was likely to be resulting

435   from the abnormally shallower thermocline in the tropical Pacific Ocean, consistent with Kutsuwada et al. (2019),

436   despite different temporal periods were considered.

437

438   *Middle layer*

439   In the middle layer between 300 300 700 m, the three datasets showed relatively poor agreement compared to the

440   upper layer. The OFES2 differed from the others by showing intense cooling before 2000 in the Atlantic Ocean (Fig.

441   9k) and moderate but consistent warming in the northern Indian Ocean over most of the whole period (Fig. 9l). In

442   addition, there were large-scale cooling patches in the northern Pacific Ocean and along the Indian Equator from the

443   OFES2, while these cooling were not apparent in the other two datasets. These cooling distributions further showed

444   where and when the cooling trend from the OFES2 in Figs. 3 occurred and can be at least partially attributed to the

445   spin-up issue of the OFES2. However, sSome similarities between the OFES2 and other two datasets emerged in

446   recent decades. For example, the OFES2 reproduced the marked warming at the high latitudes of the Atlantic Ocean

447   in the 1980s and 1990s, and a subsequent cooling (Fig. 9k), similar to the EN4 and OFES1.

448   Comparing the OFES1 with the EN4, both similarities and differences can be discerned. The OFES1 generally

449   agreed with the EN4 north to 30°N, with only a few differences. In the tropics, however, large differences were found

16

450   between the OFES1 and EN4. For instance, the OFES1 indicated that the northern Indian Ocean was cooling

451   consistently (Fig. 9h), but alternate warming and cooling appeared in the EN4 (Fig. 9d). Furthermore, the intense

452   warming and cooling patches in the southern Atlantic and Indian Oceans, respectively, shown in the OFES1 (Fig. 9g,

453   h), were not clearly visible in the EN4 (Fig. 9c, d). These potential temperature changes mainly resulted from the

454   vertical displacement of the neutral density surfaces, that is, the HV (Supplementary Information, Fig. S3). However,

455   the role of the SP cannot be ignored. This was especially clear in the southern hemisphere in the EN4. The OFES2

456   also showed that the warming of the northern Indian Ocean was largely SP-related.
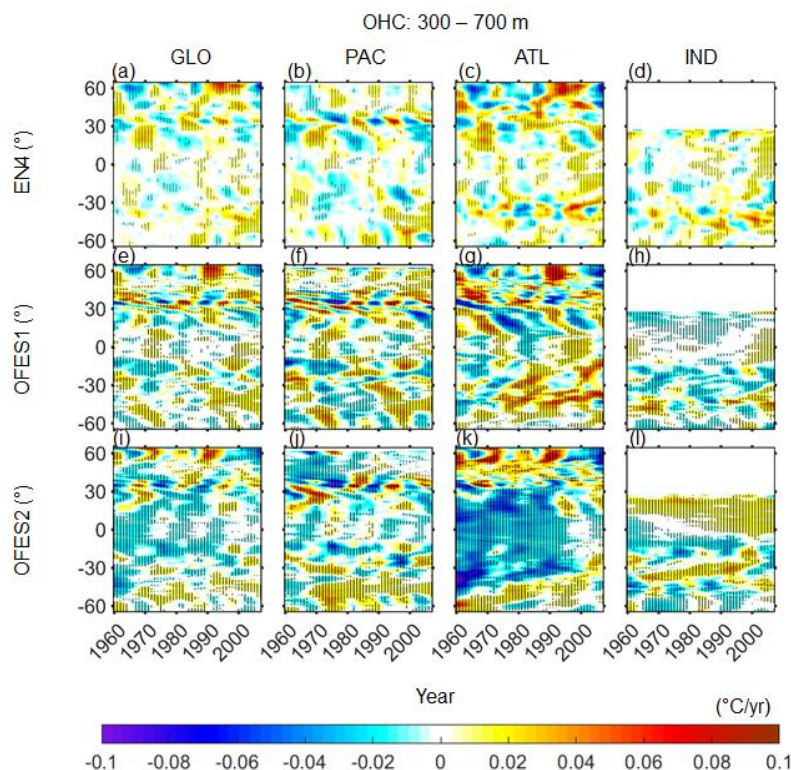
457

458   **Figure 9.** As for Fig. 8 but for the middle layer (300–700 m).

459

460   *Lower layer*

461   The northern Atlantic Ocean, especially north to 30°N, dominated the global potential temperature change in the EN4

462   (Fig. 10); this was related more to the SP, especially in the intense cooling patch (Supplementary Information, Fig.

463   S6). Although the OFES1 agreed well with the EN4 in the northern Atlantic Ocean (> 30° N), there were considerable

464   differences elsewhere between the OFES1 and EN4. More specifically, there was intense HV-associated warming

465   and cooling in the southern Pacific Ocean in the 1960s and 1970s in the OFES1, but not in the EN4 (Supplementary

466   Information, Fig. S5). In addition, the warming of the southern Pacific Ocean since about 1990 was much stronger in

467   the OFES1 than in the EN4. The main reason is that there was strong SP cooling in the southern Pacific Ocean in the

468   EN4 (Supplementary Information, Fig. S6). Moreover, the consistent cooling in the Atlantic tropics, the significant

469   warming in the southern Atlantic Ocean and the intense cooling of the northern Indian Ocean before the middle of the

470   1990s shown by the OFES1 were not evident in the EN4.

17

471 The OFES2 captured some warming patterns in the southern hemisphere, similar to the OFES1; it also agreed with

472 the other two datasets in the intense warming patch in the northern Atlantic Ocean. However, the agreement between

473 the OFES2 and the others was generally poor. Most significantly, cooling was indicated by the OFES2 at the low and

474 middle latitudes in both the Pacific and Atlantic Oceans, especially the latter. Furthermore, both the EN4 and OFES2

475 showed marked but opposite SP variations in the northern Atlantic Ocean north to 30°N, whereas the OFES1 indicated

476 moderate SP in a similar warming/cooling pattern to the EN4.

477 From Fig. 10, it seems that the spin-up may not be the primary reasons for the differences between the two OFES

478 data and the EN4, as there are no clear improvements in the agreements with the EN4 in the recent decades. Another

479 possible is that the two OFES data have not been fully spun-up even after an integration of more than 50 years for the

480 water in the lower layer.

481 To summarize, the two OFES datasets had come some good agreements with the EN4 in the upper ocean layer, but

482 largely confined to the middle-high latitudes. Poor agreements were found in the ocean beneath. Specifically, in the

483 middle ocean layer, the OFES1 had a generally reasonable agreement with the EN4 north to 30° N, but large

484 differences exist elsewhere; in the OFES2, intensive cooling patches were simulated, especially in the Atlantic Ocean.

485 Although the spin-up issue may partially explain the notable differences between the OFES data and EN4 for the

486 ocean below 300 m, other causes responsible for the examined differences are also possible.
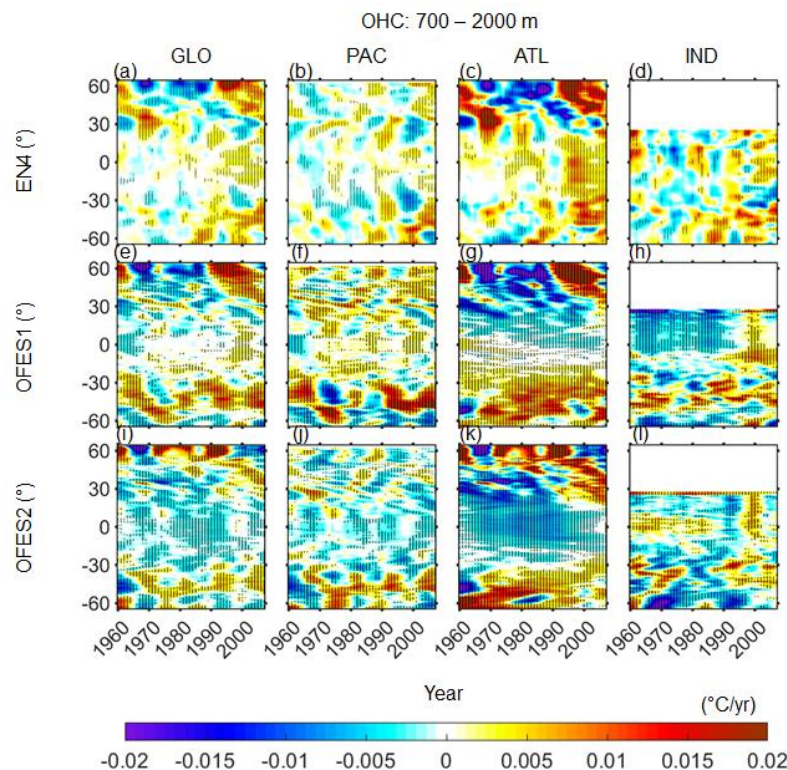
487

488 **Figure 10.** As for Fig. 8 but for the lower layer (700–2000 m). Note the different colour scales.

489

490 **3.3 Depth-time distribution of potential temperature, HV and SP trend**

491   Although we divided the top 2000 m into three layers, some detail was lost in taking layer (vertical) averages. In

492   this section, we compare ~~vertical~~ depth-time patterns of trends in the potential temperature change ($\Delta\theta_{OHC}$), and its

493   HV ($\Delta\theta_{HV}$) and SP ($\Delta\theta_{SP}$) components (Figs. 11–13).

494   For the global ocean, the upper ocean layer above 300 m accounted for most of the warming or cooling (Fig. 11,

495   left column). The EN4 showed warming over most of the investigated period with a few cooling as a response to the

496   distinctive climate events. It can be seen that the volcanic eruptions of Mount Agung and El Chichón impacted a

497   greater depth than the eruption of Pinatubo. The aforementioned strong cooling from the OFES1 in the upper Pacific

498   layer before 1990 started at a greater depth in the beginning and subsequently ending at a shallower depth (Fig. 11e).

499   At greater depths, moderate warming or cooling can be found. Specifically, in the EN4, moderate warming can be

500   seen far deep to around 2000 m since around the early 1990s. The OFES1 showed moderate warming between 500–

501   1000 m over almost the whole investigated period. Since around the middle of 1990s, a weak warming extended to

502   the 2000 m based on the OFES1. The differences of the OFES2 from the other two datasets are apparent in the global

503   ocean below around 200 m, where cooling is the dominant pattern except some weak warming patches between 500–

504   1000 m (Fig. 11i).

505   In the Pacific Ocean, the OFES2 had a generally reasonable agreement with the EN4 above around 200 m, whereas

506   the agreement between the OFES1 and the EN4 was poorer, despite of some similar warming or cooling patches.

507   Further below, the EN4 showed periodic warming and cooling. The OFES1 showed consistent warming between

508   around 500–1200 m, whereas the OFES2 estimated consistent cooling with some exceptions between 500–1000 m.

509   Although beyond the scope of this work, the question on why both the OFES1 and OFES2 showed relatively consistent

510   warming between 500–1000 m, around the depth of the permanent thermocline, necessitate a further work.

511   In the Atlantic Ocean, intense warming or cooling extended deeper when compared to the Pacific Ocean.

512   Specifically, the strong warming in the 1980–90s from the EN4 appeared as deep as around 750 m and moderate

513   warming extended to 2000 m since the middle of 1990s. The OFES1 well captured the warming in the 1970s and

514   1990s, and a subsequent cooling in the 2000s, in the upper layer of the Atlantic Ocean when compared to the EN4.

515   However, the OFES1 estimated a strong cooling in the 1980s in the upper layer of the Atlantic Ocean, which was

516   invisible in the EN4. Interestingly, the OFES1 showed a downward propagation of a strong warming from around 200

517   m to around 800 m since the early 1980s; a downward propagation of cooling from around 600 m to 1800 m can also

518   be seen in the OFES1 Atlantic Ocean (Fig. 11g). Similar to the EN4, moderate warming extended to 2000 m since

519   around the middle of 1990s. As for the OFES2, the most prominent pattern distinguishing it from the others are the

520   extensive cooling patch before around 1990. In addition, it showed moderate cooling below 1000 m before around

521   1990. These two extensive cooling patterns in the upper-middle and deep layers of the Atlantic Ocean by the OFES2

522   raised questions: what are the main causes of these two cooling patches in the OFES2 and why they suddenly stopped

523   at around 1990. One possible reason is that improvement of the reanalysis product of the atmospheric forcing since

524   1990, especially the surface heat flux and wind stress, the latter of which has been shown to be essential to the

525   subsurface temperature simulations (Kutsuwada et al. 2019).

526   In the Indian Ocean, both the OFES1 and OFES2 captured the warming in the 1960–70s and in the 2000s. However,

527   the OFES1 presented an intense cooling in the upper layer in the 1980s; a similar but less extensive cooling can also

be seen in the OFES2. Below the upper layer, the EN4 showed largely warming with a major exception of cooling in the 1970s. The two OFES presented notably different patterns. Specifically, between 500–1000 m, there were moderate warming with an intermittent in both the OFES datasets. The intermittent appeared later in the OFES2 compared to the OFES1. Below 1000 m, moderate cooling dominated before the middle of 1990s, as shown in both the OFES datasets.
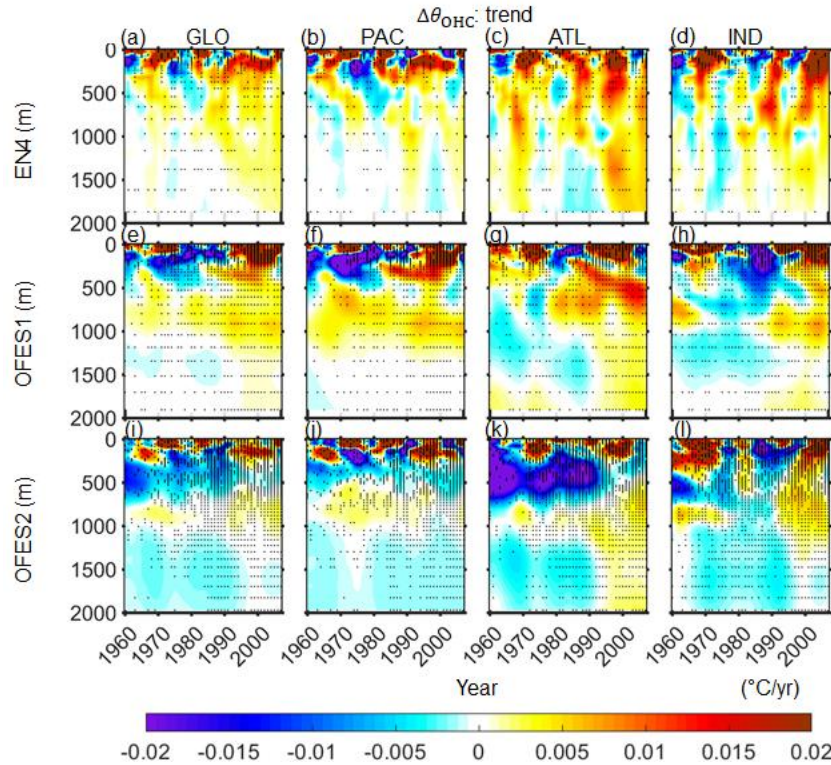
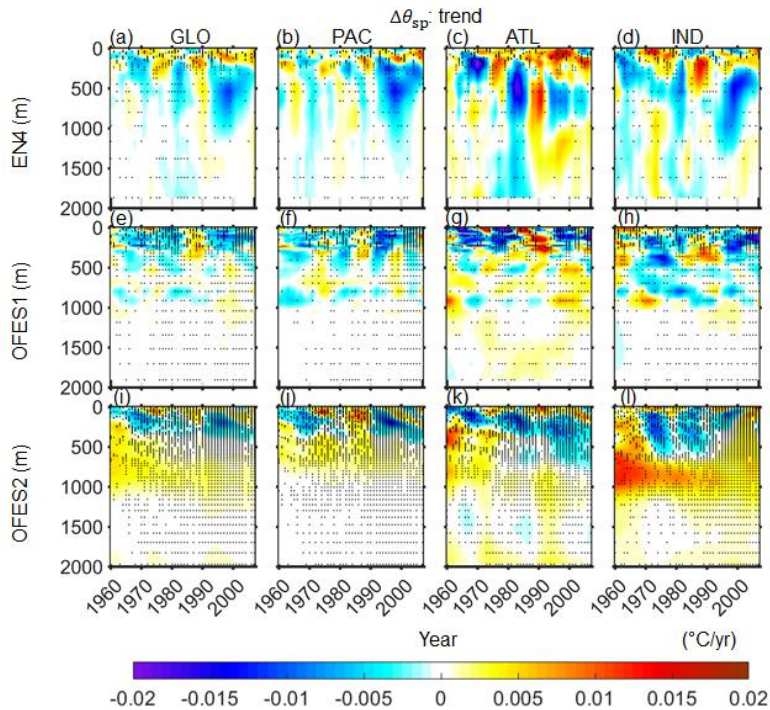**Figure 11.** Depth-time patterns of the horizontally averaged potential temperature change $\Delta\theta_{OHC}$ for (left to right) the global, Pacific, Atlantic and Indian Oceans. **Top to bottom:** EN4, OFES1 and OFES2. Horizontal axis: year; vertical axis: depth in m.

To a great extent, the HV components dominated the OHC variations by comparing the Fig. 12 with Fig. 11. For instance, the profound warming and cooling patterns in Fig. 11 were mostly associated with the HV component. Also, the moderate cooling below 1000 m in the OFES2 was also mainly related to the HV. Although the SP was generally weaker and less important than the HV in accounting for the OHC variations, its role cannot be ignored. Indeed, intense SP-associated warming or cooling were presented in the EN4 in all the major basins. The increased subsurface SP cooling since 1990s in the Pacific and Indian Oceans were particularly interesting. One speculation is that this may be related to the great increase of the subsurface salinity observations since 1990s. A possible explanation for the appearance of the prominent SP cooling in the Pacific and Indian Oceans, but not in the Atlantic Ocean is that the Atlantic Ocean has been better observed than the Pacific and Indian Oceans before 1990s. Another interesting point with regards to the SP is the consistent SP warming in the OFES2, but not visible in the other two datasets.
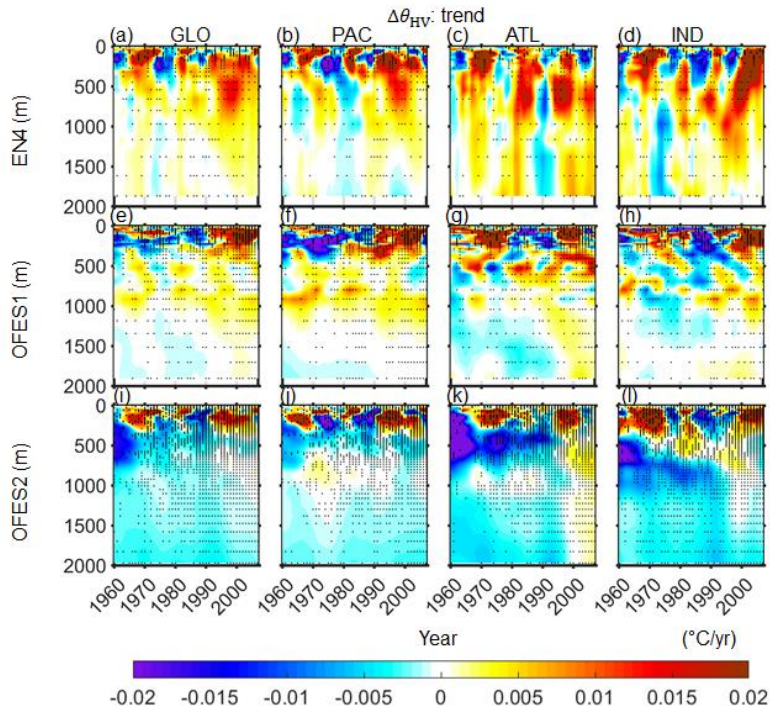
Figure 12. Depth-time patterns of the horizontally averaged potential temperature change from the HV component, $\Delta\theta_{HV}$, for (**left to right**) the global, Pacific, Atlantic and Indian Oceans. **Top to bottom:** EN4, OFES1 and OFES2. Horizontal axis: year; vertical axis: depth in m.

Figure 13. Depth-time pattern of the horizontally averaged potential temperature change from the SP component, $\Delta\theta_{SP}$, for (**left to right**) the global, Pacific, Atlantic and Indian Oceans. **Top to bottom:** EN4, OFES1 and OFES2. Horizontal axis: year; vertical axis: depth in m.

3.3 Spatial patterns of the potential temperature, HV and SP trends

To gain a more detailed understanding of the similarities and differences between the potential temperature trends from the three datasets, we presented the spatial distributions of the potential temperature change ($\Delta\theta_{OHC}$), and its HV ($\Delta\theta_{HV}$) and SP ($\Delta\theta_{SP}$) components in the three ocean layers (Figs. 14–16).

Upper layer

Warming was almost ubiquitous in the EN4 (Fig. 14a), particularly strong in the northern Atlantic Ocean and in the Southern Ocean. These two hotspots of warming were expected from both theories and models. Specifically, the shallow ocean ventilation in these two regions could warm faster than the global average (Banks and Gregory 2006; Durack et al. 2014; Fyfe 2006; Talley 2003). Major exceptions of cooling appeared in the ~~Eastern~~ Western Pacific Equator, along the north Pacific Current, in a meridional band in the southeastern Pacific Ocean, in part of the Argentine Basin and in the southern Indian tropics. All of these cooling regions consists of a small fraction of the global ocean. As with the EN4, both the OFES datasets showed significant warming in the subtropics, high-latitude of the northern Atlantic Ocean and in the Arabian Sea in the Indian Ocean. In addition, the OFES1 was similar to the EN4 in showing cooling along the north Pacific Current. Despite of these similarities, large differences exist between these three datasets. The most significant difference was in the Pacific tropics. Although, as noted earlier, there was a zonal band of cooling in the Pacific tropics in the EN4, this zonal band in the OFES1 and OFES2 was much stronger in intensity and more extensive and mainly related to the HV, especially in the OFES1.These abnormally stronger cooling pattern in the vicinity of Equator were likely to be resulting from the poor qualities of the atmospheric wind stress over some periods. As mentioned earlier, Kutsuwada et al. (2019) demonstrated that the NCEP wind stress used as the forcing of the OFES1 cause much shallower thermocline in the north Pacific tropical area and therefore significant negative differences relative to the observations. In the northeast of the Pacific Ocean, the OFES2 but not the OFES1 and EN4, showed a patch of intense cooling, corresponding to the cooling pattern in the 1960–70s (Fig. 8j). the OFES2 also showed four large cooling areas in the Atlantic Ocean (Fig. 14g). In the Indian Ocean, unlike the EN4, there was a patch of intense cooling along the western coast and in the Indian sector of the Southern Ocean from the OFES1 and OFES2, respectively.

The decomposition of the potential temperature changes into HV and SP components showed that the EN4 warming was largely the result of isopycnal deepening (HV) in the subtropics. This is consistent with the finding that the subtropical mode water (STMW) is the primary water mass accounting for global warming (Hakkinen et al., 2016), as we also show later. The SP was generally weaker than the HV, and tended to counteract the HV warming, especially in the subtropics. This dampening effect can be easily understood from Fig. 1 of Hakkinen et al. (2016). For example, in a stratified ocean with warm/salty water above cold/fresh water, typical of the subtropics, a pure warming of one water parcel can be considered as a sum of warming and salination along its original potential-temperature/salinity characteristic (HV part), and a cooling and freshening along the new isopycnal (SP). Two major exceptions were the northern Atlantic subtropics and the Indian Ocean, where SP was mostly warming. The SP warming in the northern Atlantic subtropics results from a large salinity increase through evaporation (Curry et al., 2003; Hakkinen et al., 2016). Similarly, we found that positive SP warming also occurred in most of Indian Ocean, except west to the

southwest Australia. Indeed, this SP-related warming in the northern Indian Ocean dominated the potential temperature change, especially in the Arabian Sea. The most significant SP warming, however, was found in the Indian sector of the Southern Ocean (may be related to the freshening of the Southern Ocean), in the southern subtropics of the Atlantic Ocean and in the Labrador Sea (Fig. 14c).
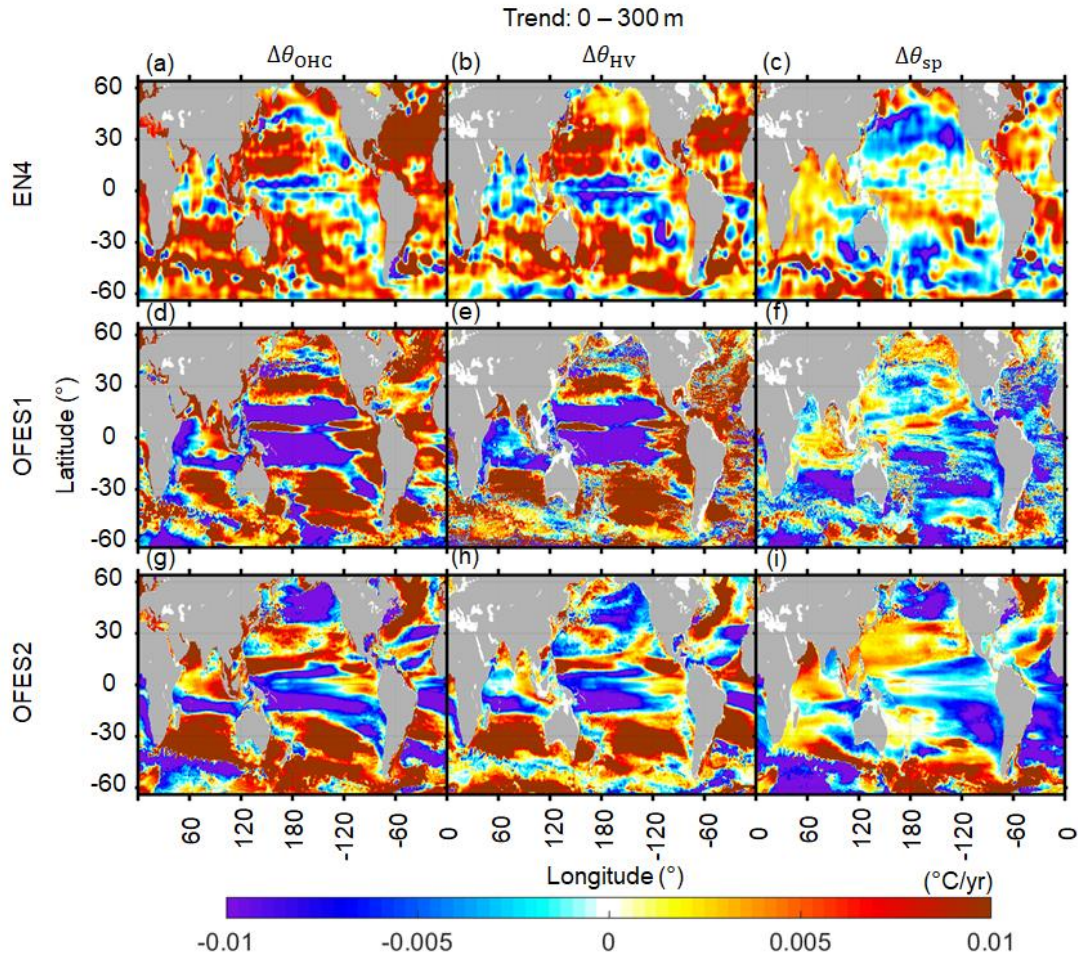
Figure 14. Spatial distributions of $\Delta\theta_{OHC}$ (**top row**), $\Delta\theta_{HV}$ (**middle row**) and $\Delta\theta_{SP}$ (**bottom row**), 1960–2016, in the top ocean layer (0–300 m). Left to right: EN4, OFES1 and OFES2. Standard deviations of $\Delta\theta_{OHC}$, $\Delta\theta_{HV}$ and $\Delta\theta_{SP}$ are given in the Supplementary Information.

Comparing the HV components in the three datasets showed that the two OFES simulations were able to reproduce the subtropical HV warming pattern, although less accurately in the northern Pacific subtropics. The strong and extensive equatorial cooling in the Pacific and Indian Oceans was largely associated with the HV in the two OFES datasets.

The SP in the OFES1 was similar to the EN4 in the northern subpolar region of the Pacific Ocean, in part of the northern Pacific subtropics, in the Labrador Sea and in part of the northern Indian Ocean. The OFES2 SP was similar to the EN4 in the Labrador Sea and the western Indian Ocean. In general, however, there were no common patterns in most of the global ocean. In particular, neither of the OFES datasets captured the SP warming in the northern Atlantic subtropics, and the OFES2 indicated moderate SP warming in the north Pacific subtropics and intense SP

23

warming in the Pacific sector of the Southern Ocean, respectively. The improvements of SP from the OFES1 over that from the OFES1 in the Arabian and Indonesian Seas but not in the Bengal Bay was consistent with the S2020, to some extent. The authors demonstrated smaller bias in the water properties in the Arabian and Indonesian Seas, but large salty bias remained in the Bengal Bay in the OFES2.

In Fig. 3, we showed that the SP was highly similar between the EN4 and OFES2 in the upper layer of the Pacific Ocean. However, the spatial distributions of the SP component in the Pacific Ocean were seldomly similar between the EN4 and OFES2. That is, the time series of a basin-wide quantity hides many details.
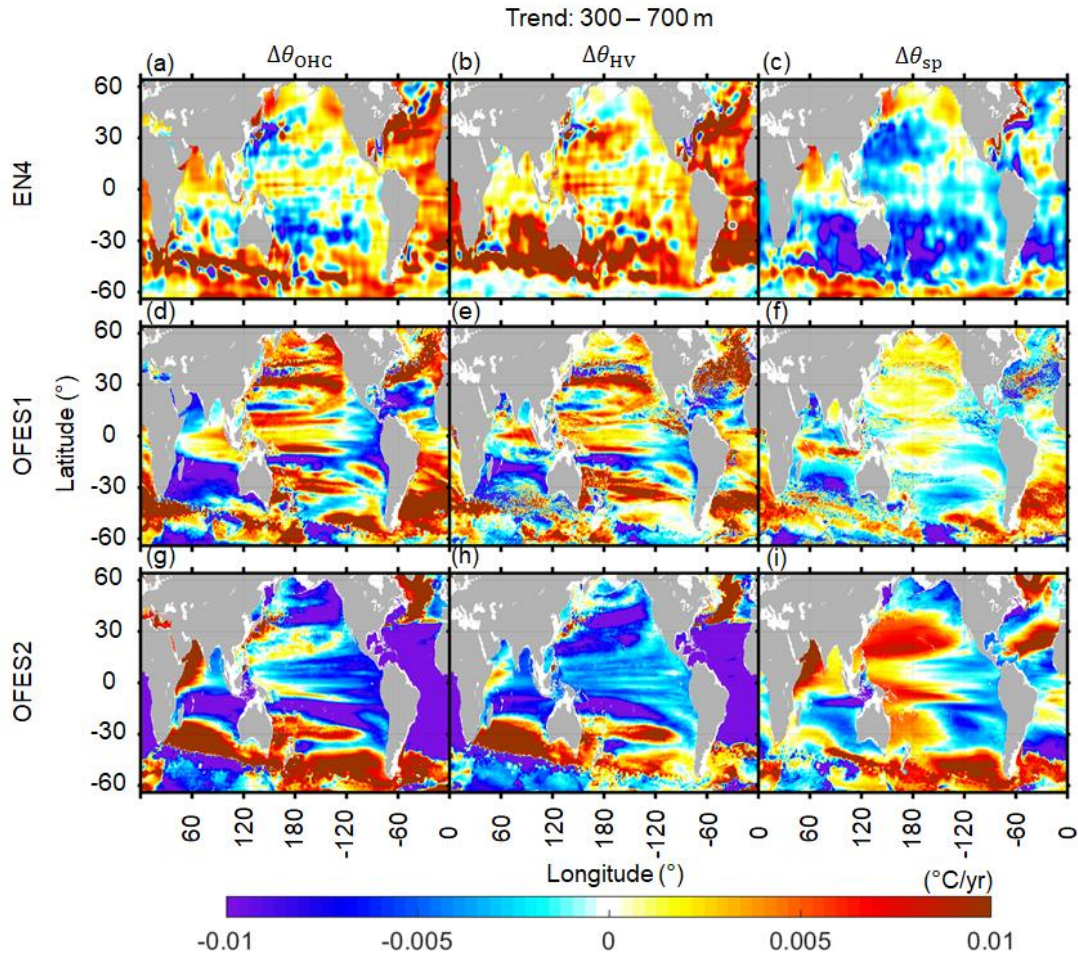
Middle layer

The EN4 showed cooling in the ocean, concentrated in the southern Pacific subtropics and in the region associated with the Kuroshio (Fig. 15a). For the rest of the global ocean, especially over the bulk of the Atlantic Ocean, in the northern Indian Ocean and along the ACC path in the Southern Ocean, clear warming was presented, accompanied by sporadic cooling patches. The OFES1 could reproduce some warming patterns in the northern Pacific Ocean, the bulk of the Atlantic Ocean, in the eastern part of the northern Indian Ocean and parts of the ACC path. However, notable differences can be found between the OFES1 and EN4. Among these differences, the most prominent is the intense cooling in the southern Indian Ocean from the OFES1, which was found to occur in the 1990s from Fig. 3(d). In addition, strong cooling patches were also found in the southern Pacific tropics, west to the central-south America, in the northern Atlantic subtropics, in the Arabian Sea and along the parts of southern edge of the ACC. The pattern in the OFES1 Pacific Ocean clearly appears as zonal bands, but this zonality property was obscure in the EN4. Consistent with Fig. 3, intense cooling was simulated in all the major basins by the OFES2, with most prominent in the Atlantic Ocean. Besides these notable cooling patches, large-scale strong warming patterns were found in the Kuroshio region, in the southern Pacific and Indian subtropics, in the northern Atlantic Ocean (north to 35° N), in the western part of the northern Indian Ocean and in the Pacific and Atlantic sectors of the Southern Ocean. In general, over the bulk of the global ocean, there were apparent differences between these three datasets. The above 700 m was relatively well observed, especially in the Atlantic Ocean (even back to 1950–60s, Hakkinen et al., 2016). Therefore, it is likely that the OFES2 was the outlier at this multi-decadal scale and there were some potential problems in the OFES1, for example, in the southern Indian Ocean.

Interestingly, the HV warming was almost ubiquitous in the middle layer from the EN4 (Fig. 15b), especially in the Southern Hemisphere, consistent with the warming shift towards to the Southern Hemisphere found in Hakkinen et al. (2016). Correspondingly, the SP cooling also occupies most of the global ocean (Fig. 15c), with a similar southern shift, most prominent to the east and west of the Australia. The major SP warming patches were found in the Sea of Okhotsk, north to the Gulf Stream, in the Arabian Sea and along the southern edge of the ACC. These regions are generally associated with strong salinity variations. Comparing the HV and SP between the EN4 and OFES1 showed that the OFES1 captured some warming patterns in the Pacific and Atlantic, but not the Indian, subtropics. The HV agreement in the southern Pacific and Indian tropics and in the Southern Ocean were mostly poor. As for the SP, the OFES1 reproduced the intense SP cooling west to the Australia and in the southern Pacific subtropics, despite of smaller coverage compared to the EN4. However, the OFES1 showed almost opposite SP trends over most of the global ocean. In the OFES2, both the HV and SP were strong, but the basin-wide cooling was mainly the result of HV.

649   Overall, the OFES2 had a reasonable agreement with the EN4 in the southern subtropics (Pacific and Indian Oceans)

650   in terms of HV. It also had a common HV warming patch in the northern Atlantic Ocean (north to 35° N) as the EN4.

651   With regards to the SP, the OFES2 was similar to the EN4 in showing SP warming in the Arabian Sea and parts of

652   the southern edge of the ACC. Also, it captured the SP cooling in the eastern Pacific Ocean, along the Gulf Stream

653   path, west to the Australia. Except of these similarities, however, the OFES2 was generally opposite to the EN4.


654

655   **Figure 15.** As for Fig. 14 but for the middle layer (300–700 m).

656

657   *Lower layer*

658   The warming and cooling intensities were generally much weaker than in the top two layers, consistent with many

659   previous findings that more ocean heating occurs in the upper 700 m than at greater depths (Hakkinen et al., 2016;

660   Levitus et al., 2012; Wang et al., 2018; Zanna et al., 2019). The EN4 showed widespread warming patches in the

661   Southern and Atlantic Oceans, as well as three large zonal bands of cooling in the southern subtropics of the Pacific

662   and Indian Oceans, and in the northern subpolar region of the Atlantic Ocean (Fig. 16a). Similar to the EN4, warming

663   was seen along the northern edge of the ACC and in the southern Atlantic Ocean in the OFES1, but with much stronger

664   intensity than the EN4 (Figs. 16a, d). There was also moderate warming over almost the whole Pacific Ocean in the

665   OFES1. Significant differences between the OFES1 and EN4 were found in the northern Atlantic Ocean, where the

666   OFES1 showed extensive cooling compared to the moderate warming in the EN4. There was also strong cooling in

25

the OFES1 Arabian Sea, in contrast to the quite weak warming in the EN4 Arabian Sea. To some extent, the OFES2 was similar to the other two in showing warming along the northern edge of the ACC and in the southern Atlantic Ocean south to 30°S (Fig. 15g), despite of the intensity differences. It also showed cooling in the low and middle latitudes of the Atlantic Ocean, as did the OFES1 but opposite to the EN4. However, the bulk of the Pacific Ocean was shown to be cooling in the OFES2, which was almost opposite to the OFES1 (Fig. 15d) and only similar to the EN4 in part of the southern Pacific subtropics (Fig. 15a). Moreover, intense and widespread cooling appeared in the Indian sector of the Southern Ocean in the OFES2. The warming of the northern ACC was captured by the OFES2.
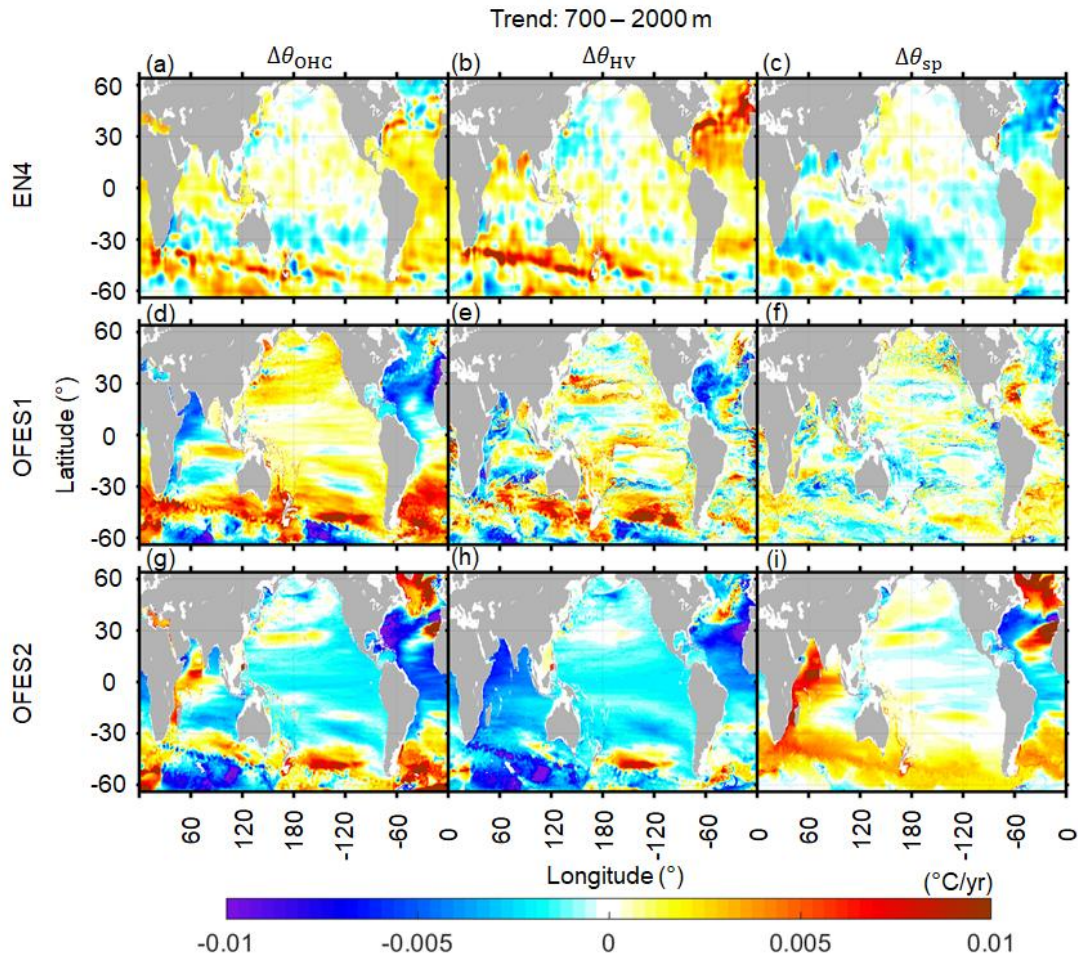
Figure 16. As for Fig. 14 but for the lower layer (700–2000 m).

In the NE4, there was intense HV warming along the northern edge of the ACC in the Indian and Pacific Oceans, and in the northern Atlantic Ocean (Fig. 16b), which largely accounted for the total potential temperature variations and were generally accompanied by SP cooling (Fig. 16c). In the northern Atlantic tropics and southern Atlantic Ocean, moderate HV and SP warming coexist. We found that the ~~OFES2~~ OFES1 captured the HV warming pattern along the northern edge of the ACC, being consistent with the EN4. However, there were remarkable differences from the EN4, particularly in the northern Atlantic and Indian Oceans. As for the SP, there were some similarities between the OFES1 and EN4, for example, they both had SP cooling and warming in the northern and southern Atlantic Ocean, respectively. Among the three datasets, the OFES2 showed the most extensive and strong but generally cooling in the

685 HV component, except a patch of HV warming in the Pacific sector of the Southern Ocean, and such a warming patch

686 was also seen in the EN4. In contrast, intense SP warming was estimated in the OFES2 in the Southern Ocean, in the

687 western Indian Ocean, in the northern Atlantic subpolar regions and a large-scale patch of abnormally strong SP

688 warming associated with the Mediterranean Overflow Water (MOW). This very strong SP warming related to the

689 MOW is likely the result of the unrealistic spreading of salty Mediterranean overflow found in **S2020**.

690   Besides the above-discussed multi-decadal linear trend, we have demonstrated that (not shown here) the significant

691 differences between the two OFES datasets and the EN4 were much reduced if we considered only the period between

692 2005–2016, which was argued to be well spun-up by **S2020**. In addition, over this 12-year period, the spatial pattern

693 of the OFES2 did show some improvements over the OFES1 for upper and middle layers, but not necessarily for the

694 lower layer, when taking the EN4 as a reference. Does this better agreement come from a better spun-up or come from

695 the improvements of the reanalysis product of the atmospheric forcing for these two OFES data? This interesting

696 question would require a further detailed exploration in the future.
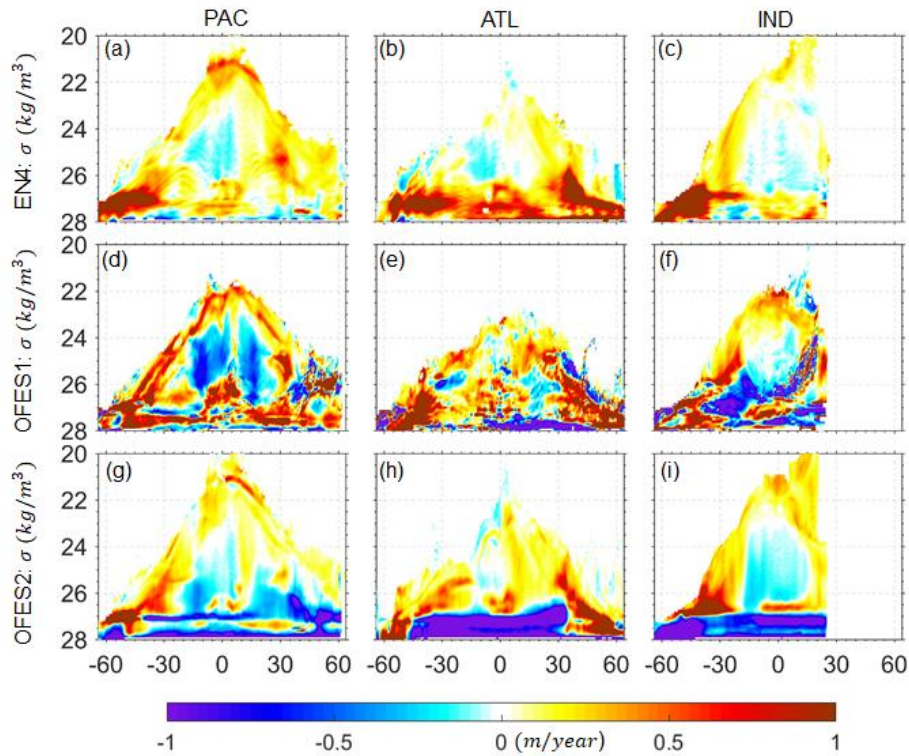
3.4 Trends in the HV and SP in the neutral density domain

698 To analyse the warming and cooling from the perspective of ~~water~~ water-mass, it is useful to show the HV and SP

699 components in neutral density coordinates, as suggested by one reviewer. Following Hakkinen et al. (2016), we

700 calculated the linear trend (over 1960–2016) in the zonal-averaged sinking of the neutral density surfaces in each

701 major basin (Fig. 17) and the SP-related warming or cooling along the neutral density surfaces (Fig. 18).

702   Our results based on the EN4 were similar to those of Hakkinen et al. (2016), using the EN4, although they used

703 an earlier EN4 version (EN4.0.2) and considered the period over 1957–2011. Specifically, our EN4 results similarly

704 showed that the bulk of HV warming (deepening of neutral density surfaces) was associated with a ~~water~~ water-mass

705 of over 26 kg/m^3, and mainly concentrated south to 30° S, to wit, from the ventilation region at high latitudes to the

706 subtropics. There was one exception in the Atlantic Ocean, where warming also occurred at the low-middle latitudes

707 and in the northern Atlantic Ocean. The concentrated warming in the northern Atlantic Ocean was attributed to the

708 phase change of North Atlantic Oscillation (NAO) from negative in the 1950–60s to positive in the 1990s (Hakkinen

709 et al. 2016; Williams et al. 2014). As explained in Hakkinen et al. (2016), these significant deepening of neutral density

710 surfaces were associated with the Subtropical Mode Water (STMW, $26.0 < \sigma_0$ (kg/m^3) < 27.0) and the Subantarctic

711 Mode Water (SAMW, $26.0 < \sigma_0$ (kg/m^3) < 27.1). These vertical displacements of neutral density surfaces may have

712 resulted from heat uptake via subduction, which then spread from these high-latitude ventilation regions. The large

713 vertical deepening of the STMW and SAMW would then push the Subpolar Mode Water (SPMW, $27.0 < \sigma_0$ (kg/m^3)

714 < 27.6) and Antarctic Intermediate Waters (AAIW, $27.1 < \sigma_0$ (kg/m^3) < 27.6) down. However, as the vertical

715 displacement of the STMW/SAMW was larger, its volume would have therefore increased and the volume of the

716 underlying SPMW/AAIW decreased (Hakkinen et al., 2016). Besides these significant sinking of neutral density

717 surfaces, there was generally a shoaling pattern of lower density (σ_0 (kg/m^3) ranging from 24–26), and mainly

718 concentrated between the Equator and 30° S. To a large extent, this shoaling occurred in the central water, for example,

719 the South Pacific Central Water (SPCW).

720   Here, our focus is not on the detailed mechanisms of warming from the perspective of water mass, as it was in

721   previous studies. Instead, we focus on the differences between the datasets in the trends of the HV and SP.

722   It can be seen that along the surfaces of the Pacific and Indian Oceans, there was generally an apperance of HV

723   warming in almost all the three datasets. In the Atlantic Ocean, however, the EN4 estimated a sea surface cooling

724   south to 30° S and in the northern tropics; the OFES2 also estimated a cooling trend ~~in~~ near the surface of the Atlantic

725   tropics. Different from both the EN4 and OFES2, the OFES1 showed an intense HV cooling pattern along the Atlantic

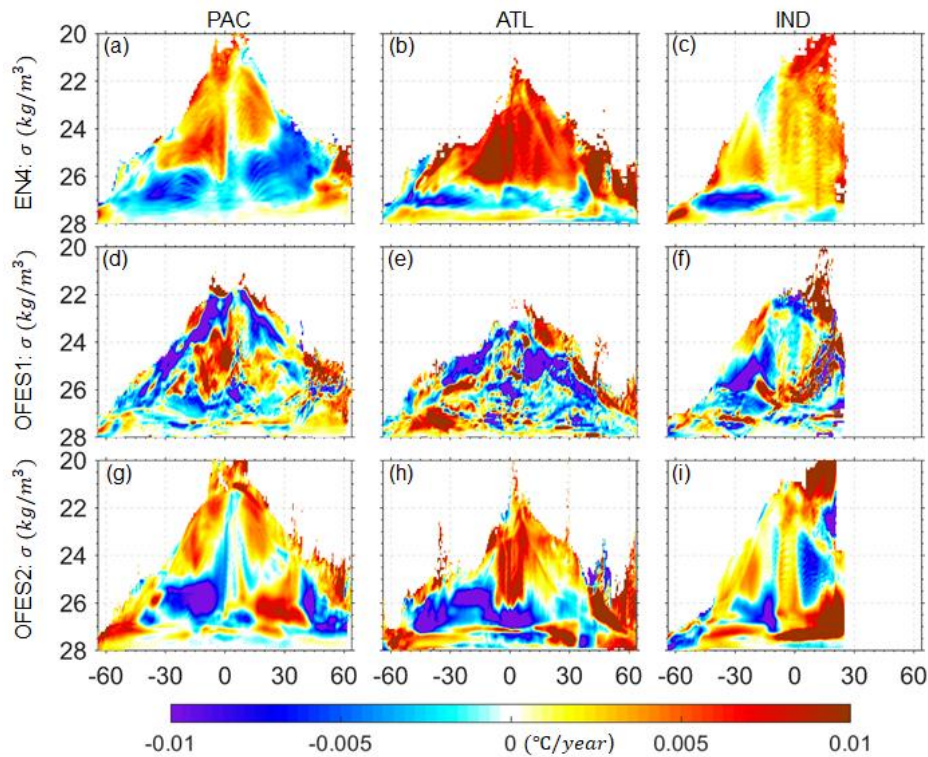726   surface between around 30–50° N (Fig. 17e).

727

Figure 17. Linear trends in the zonal-averaged sinking of the neutral density surfaces in the Pacific (**left column**), Atlantic (**middle column**) and Indian (**right column**) Oceans. **Top to bottom:** EN4, OFES1, OFES2. Positive values mean deepening of the neutral density surfaces. The calculation was for the water above 2000 m.

731

732   South to 30° S, large downward movements associated with the STMW, SAMW and AAIW were found in all the

733   three basins in the EN4; in the OFES1, the dominant pattern in the three basins was sinking but was surrounded by

734   shoaling patches; larger differences from the EN4 were found in the OFES2, which showed significant and extensive

735   shoaling patterns, especially in the Indian Ocean. The almost opposite trend in the vertical displacements of the neutral

736   density surfaces between the OFES2 and the observational-based EN4 may indicate that the ~~water~~ water-mass

737   properties simulated in the OFES2 were unrealistic, at least at this multi-decadal scale.

738   In the ocean interior between 30°S and 30° N, the OFES1 presented shoaling patterns in the ~~northern and southern~~

739   Pacific and Indian Oceans, but not prominent in the Atlantic Ocean. Although these shaoling patterns in the Pacific

740   and Indian Oceans were also seen in the EN4, as noted eailer, the magnitude in the EN4 was generally much smaller.

741   The OFES2 had a better agreement with the EN4 in the shoaling pattern in the southern Pacific subtropics. It also

742 captured the shoaling in the EN4 Indian Ocean, with a similar coverage but generally stronger. The shoaling in the

743 southern Atlantic subtropics was not typical in the OFES2, similar to the OFES1 but different from the EN4.

744   North to 30° N, sinking was widespread in the EN4, particularly strong in the northern Atlantic Ocean. This very

745 strong sinking in the northern Atlantic Ocean came mainly from the SPMW and STMW. In the EN4 Pacific Ocean,

746 there was some shoaling patches, which was related to the North Pacific Intermediate Water (NPIW), and to a large

747 extent, corresponded to the HV cooling in Fig. 16(b). In the OFES1, the pattern was filled with both sinking and

748 shoaling patches and defies easy intepretation. However, an apparent outlier is the intense shoaling in the OFES1

749 northern Atlantic Ocean (mainly below 700 m from Figs. 14–16), just opposite to the EN4. The shoaling of neutral

750 density surfaces in the OFES2 Pacific Ocean north to 30° N was even more prominent than in the OFES1. The OFES2

751 had a better agreement with the EN4 in the sinking patterns in the Atlantic Ocean north to 30° N.

Figure 18. Linear trends in the zonal-averaged warming or cooling along the neutral density surfaces in the Pacific (**left column**), Atlantic (**middle column**) and Indian (**right column**) Oceans. **Top to bottom:** EN4, OFES1, OFES2.

756   The major SP warming in the EN4 Pacific Ocean was associated with the STUW and Pacific Central Water in the

757 low and middle latitudes, with a shift towards to the southern hemisphere. The northern high-latitude SP warming was

758 mainly related to the Pacific Subarctic Intermediate Water (PSIW). The two SP cooling came from the STMW,

759 corresponding to the sinking pattern in Fig. 17(a). This HV warming / SP cooling was particularly typical in the

760 subtropical regions and the HV warming / SP warming was typical in the subpolar regions, as noted above and more

761 details were presented in Hakkinen et al. (2016). Very strong SP warming occurred in the Atlantic Ocean, resulting

762 from salination via the evaporation process. In the southern Atlantic Ocean, pattern of SP cooling is mostly associated

763 with the sinking of STMW.

764   The SP pattern from the OFES1 was quite noisy and had generally poor agreements between the OFES1 and the
765   EN4 in terms of SP warming, which is likely to be resulting from some issues of salinity simulation in the OFES1. As
766   shown in S2020, the OFES1 was not capable of simulating salty outflows, for example, the outflow through the Persian
767   Gulf into the Indian Ocean. There were notable improvements in the salinity field in the OFES2 over OFES1, mainly
768   attributed to the inclusion of river runoff and a sea-ice model, but some issues still remained, e.g., poor performance
769   in the simulation the Mediterranean outflow. Overall, the SP warming pattern in the density coordinate was
770   significantly improved in the OFES2 when compared to the OFES1. When combing Figs. 14–16, however, one can
771   see that the similarities in the SP estimation between the OFES2 and the EN4 was confined to small fraction of the
772   global ocean, mainly in the upper and middle layers of the Labrador Sea and the northern Indian Ocean in the Southern
773   Ocean. In addition, the OFES2 was also similar to the EN4 in showing a patch of SP cooling in the western part of the
774   northern Atlantic subtropics.
775
776   **3.5 A basin-wide heat budget analysis**
777   The fundamental mechanisms controlling the oceanic thermal state include the net surface heat flux, the zonal and
778   meridional heat advections in the horizontal direction and the vertical heat advection and diffusion (Fig. 1b). Lateral
779   heat diffusion was not considered here, as it was found to play a minor role from our analysis (not shown). Since our
780   focus is on the global and basin-wide OHC in the three vertical layers, we calculated and compared the inter-basin
781   heat exchange, and the vertical heat advection and diffusion, integrated over each basin from 1960–2016. No vertical
782   heat diffusivity data were available from the OFES1, and the vertical heat diffusivity from the OFES2 was temporarily
783   unavailable due to a security incident. This prevented us from calculating the vertical heat diffusion directly. As an
784   alternative, we calculated the residual of the OHC change and all the related heat transport into each basin, and took
785   it as a proxy for the vertical diffusion. This indirect method may suffer from some errors, for instance, it includes the
786   impacts of river runoff in the OFES2, but can still provide us with important information. Our calculations are listed
787   in Tabs. 2–4. The related time series of these surface heat flux and heat advection were shown in the supplementary
788   Figs. S7–9.
789
790   *Upper layer*
791   In the Pacific Ocean, the changing rate of the time-averaged OHC was rather low in both the OFES1 and OFES2.
792   However, the averaged surface heat flux in the OFES1 was twice that in the OFES2, indicating that more heat was
793   injected to the OFES1 Pacific Ocean and signifying the differences in the atmospheric forcing. Vertically, both
794   indicated a net downward advection of heat in the Pacific Ocean at 300 m, but much stronger intensity in the OFES1
795   (different by around 0.7 W/m^2); this may be related to their different wind-forcing sources, as the downward heat
796   advection in the upper ocean was mainly from the wind-driven Ekman pumping in the subtropical gyres. Indeed,
797   Kutsuwada et al. (2019) claimed that the NCEP wind stress curl was too strong and caused overly strong Ekman
798   pumping. There was 0.150 W/m^2 more eastward heat advection through the water passage between the Australian
799   mainland and 64° S (P3 in Fig. 1a) in the OFES2. Although the MHA from the Southern Ocean to the Pacific Oceans
800   (P4) was of opposite sign in the two OFES datasets, the relatively small absolute value indicated that this difference

801   was slight. The Drake Passage (P5) is the major water passage through which heat is exchanged between the Pacific
802   and Atlantic Oceans. There was 0.108 W/m^2 more heat loss through the P5 into the Atlantic Ocean in the OFES1,
803   inferring a stronger ACC from the OFES1 in the upper ocean. The P7 and P8 connect the Pacific and the Indian
804   Oceans; the Indonesian Throughflow (ITF) flows through the P7. The MHA through the P7 was almost two times
805   stronger in the OFES2 than in the OFES1, with a difference of 0.637 W/m^2. This indicated an enhancement of the IFT
806   simulated by the OFES2, which agreed well with Sasaki et al. (2018), who showed that the inclusion of a tidal-mixing
807   scheme resulted in an intensification of the ITF, remembering that the a tidal-mixing scheme was implemented in the
808   OFES2 but not OFES1. In addition, the OFES1 showed more heat transported westward into the Indian Ocean between
809   Papua New Guinea and Australia (P8) but the small absolute heat advection indicated that it was not the major cause
810   of the OHC discrepancy between the OFES1 and OFES2. The net heat advection through the Bering Strait (P9) was
811   rather weak in both datasets. The indirect calculation of the VHD showed that there was net downward heat diffusion
812   at a depth of 300 m in the Pacific Ocean in both the two OFES datasets but with a much stronger intensity (different
813   by 0.747 W/m^2) in the OFES1.

814   In the Atlantic Ocean, the OHC increased at an average rate of 0.032 W/m^2 in the OFES1 but decreased by 0.014
815   W/m^2 in the OFES2. There was net surface heating in the OFES1 Atlantic Ocean but minor cooling in the OFES2.
816   The two OFES datasets were also profoundly different in the VHA at 300 m. Specifically, the OFES1 showed a net
817   downward heat advection, the OFES2 an upward and much weaker heat advection. Again, this difference in the VHA
818   was likely the result of different wind stress datasets in the two OFES, as discussed above. The OFES1 showed 0.158
819   W/m^2 more heat transported from the Atlantic Ocean to the Indian Ocean through the P1 between the South Africa
820   and 64° S. As mentioned above, more heat was advected into the Atlantic Ocean through the Drake Passage (P5) in
821   the OFES1. Additionally, there was more heat advected southward from the Atlantic Ocean to the Southern Ocean in
822   the OFES1 (P6). The wide passage connecting the north Atlantic Ocean to the Arctic Ocean (P10) also served as the
823   major channel through which the Atlantic Ocean exchanged heat; the two OFES datasets gave similar heat loss. All
824   these differences combined led us to conclude that the respective values for the vertical heat diffusion at 300 m differed
825   by 0.411 W/m^2 (more upward heat diffusion in the OFES1).

826   In the Indian Ocean, the averaged OHC increasing rate was 0.009 W/m^2 higher in the OFES2 than in the OFES1.
827   The time-averaged surface heat flux in the OFES2 was 0.729 W/m^2 less than that in the OFES1. Both datasets showed
828   a net downward heat advection but that in the OFES2 was around three times stronger. The small difference in the
829   southward heat advection across the 64° S (the P2) only affected the OHC in the upper Indian Ocean to a small extent.
830   In contrast, the differences in the HF, VHA and the MHA associated with the ITF contributed to the difference and
831   led us to calculate a remarkable discrepancy of 1.898 W/m^2 in the VHD at a depth of 300 m in the Indian Ocean. The
832   enhanced ITF is one of the main contributors to the larger OHC increase in the upper layer of the OFES2 Indian Ocean
833   (Fig. 2).

834   To summarize, there was generally more surface heat flux into the major basins in the OFES1. The vertical heat
835   advection was generally downward, indicating the essential role of the subtropical Ekman pumping in the heat uptake
836   in the upper ocean layer. The differences of these two (HF and VHA) were mainly from the different atmospheric
837   forcing used in the two OFES datasets, emphasizing the importance of reliable atmospheric forcing product in the

numerical ocean modelling. Although the different wind stress could also produce different lateral advections through the P1–P10, the local-integrated differences were generally smaller than the basin-integrated differences. The most prominent difference in the lateral heat advection was associated with the ITF, mainly as a result of the adoption of a tidal-mixing scheme. This ITF-related difference and the indirectly inferred VHD suggested the significance of vertical mixing scheme in producing the examined differences of OHC.

Table 2. Time-averaged OHC, surface heat flux (HF) and advection of heat through the major water passages for the upper layer of each basin (0–300 m). VHA is at a depth of 300 m. Residual: difference between the OHC increase and all the heat flux into a basin, approximately the vertical diffusion of heat. All quantities converted to W/m^2 applied over the entire surface of the Earth. Values smaller than 0.001 are set to 0. Positive means heat gain and negative means heat loss.

PACIFIC OCEAN (0–300 m)									
	OHC	HF	VHA	P3	P4	P5	P7	P8	P9	Residual
OFES1	–0.025	2.135	–0.814	1.233	0.011	–0.891	–0.728	–0.162	–0.003	–0.808
OFES2	0.007	1.066	–0.113	1.383	–0.020	–0.783	–1.365	–0.100	0	–0.061

ATLANTIC OCEAN (0–300 m)							
	OHC	HF	VHA	P1	P5	P6	P10	Residual
OFES1	0.032	0.184	–0.445	–0.823	0.891	–0.085	–0.440	0.749
OFES2	–0.014	–0.036	0.005	–0.665	0.783	–0.051	–0.388	0.338

INDIAN OCEAN (0–300 m)							
	OHC	HF	VHA	P1	P2	P3	P7	P8	Residual
OFES1	0.026	0.195	–0.639	0.823	–0.038	–1.233	0.728	0.162	0.028
OFES2	0.035	–0.534	–2.091	0.665	–0.012	–1.383	1.365	0.100	1.926

Middle layer

There were no significant differences between the OFES1 and OFES2 in the horizontal and vertical heat transports in the middle layer (300–700 m) of the Pacific Ocean (Tab. 3). It can be seen that the IFT was weak for this depth layer and its differences between the OFES1 and OFES2 was small (0.084 W/m^2). However, heat was advected or diffused from the upper layer (at 300 m, the top face of the middle ocean layer). There was a difference of around 0.747 W/m^2 in the VHD at a depth of 300 m in the Pacific Ocean and a difference of 0.701 W/m^2 in the VHA. All these together led us to infer a VHD difference of 1.295 W/m^2 at a depth of 700 m in the Pacific Ocean, with more heat was diffused downward in the OFES1.

In the Atlantic Ocean, the averaged OHC trend was positive in the OFES1 but negative in the OFES2, different by 0.129 W/m^2. A VHA of –1.585 W/m^2 was calculated for the OFES2, 32% stronger than that for the OFES1. Additionally, more heat was lost through the P1 into the Indian Ocean and more heat was advected into the Atlantic Ocean through the Drake Passage in the OFES1. Differences also existed in the heat advection between the Atlantic Ocean, and the Southern (P6) and the Arctic (P10) Oceans. The vertical heat transport (VHA + VHD) at the 300 m of the Atlantic Ocean (Tab. 2) was close from the two OFES data. The resulting inferred VHD through the depth of 700 m in the Atlantic Ocean was upward in both datasets but 0.393 W/m^2 stronger in the OFES2.

The averaged OHC trend in the Indian Ocean was weakly negative in both the OFES1 and OFES2. 0.142 W/m^2 more heat was advected downward at a depth of 700 m in the OFES2. Horizontally, 0.121 W/m^2 more heat was

866 acquired from the Atlantic Ocean (through the P1) in the OFES1 but there were neglectable differences in the lateral

867 heat transport through the others passages connecting the Indian Ocean with the other basins. The time-averaged VHD

868 at 700 m in the Indian Ocean was 0.423 W/m^2 in the OFES1 and 1.083 W/m^2 in the OFES2.

869   To summarize, the notable cooling trend in the Pacific and Atlantic Ocean (Fig.3) from the OFES2 came mainly

870 from the vertical heat transport (VHA + VHD) processes. For example, there was a net upward heat advection at 300

871 m in the OFES2 Atlantic Ocean and a stronger downward heat advection at 700 m, as a result, more heat was lost

872 vertically in the middle layer of the OFES2 Atlantic Ocean compared to the OFES1 Atlantic Ocean.

873

874 **Table 3.** As for Tab. 2 but for the middle layer (300–700 m). VHA is at a depth of 700 m.

	PACIFIC OCEAN (300–700 m)							
	OHC	VHA	P3	P4	P5	P7	P8	P9	Residual
OFES1	0.017	–0.096	1.208	–0.026	–1.056	0.044	0	0	–1.679
OFES2	–0.034	–0.084	1.247	–0.030	–0.917	–0.040	0	0	–0.384

	ATLANTIC OCEAN (300–700 m)						
	OHC	VHA	P1	P5	P6	P10	Residual
OFES1	0.037	–1.203	–0.770	1.056	0.056	–0.057	1.260
OFES2	–0.092	–1.585	–0.649	0.917	0.017	–0.102	1.653

	INDIAN OCEAN (300–700 m)						
	OHC	VHA	P1	P2	P3	P7	P8	Residual
OFES1	–0.010	–0.519	0.770	–0.043	–1.208	–0.044	0	0.423
OFES2	–0.013	–0.661	0.649	–0.043	–1.247	0.040	0	1.083

875

876 *Lower layer*

877 Consistent with Fig. 4, the OFES2 showed cooling in the bottom (700–2000m) layer of each basin, but the OFES1 an

878 overall warming (Tab. 4). In the Pacific Ocean, the VHA at 2000 m was downward and of similar magnitude in the

879 two OFES datasets. Due to the vertical coherence of the ACC, there was intense eastward heat advection through the

880 P3 and P5, even below 700 m, with the OFES2 showing greater advection. The horizontal heat advection through the

881 P4 and P7 was relatively weak but again larger in the OFES2. For example, the MHA through the P7 was more than

882 two times larger in the OFES2. In fact, more heat advected southward into the Indian Ocean through the ITF was

883 found in all the ocean layers (the OFES1 showed a weakly northward heat advection in the middle layer). As a result

884 of these differences, and the VHA and VHD at a depth of 700 m, we calculated a significant difference in the VHD

885 between the two OFES datasets at a depth of 2000 m in the Pacific Ocean of around 1.252 W/m^2 in the downward

886 direction.

887   Unlike at 2000 m in the Pacific Ocean, there was much stronger downward heat advection at 2000 m in the OFES2

888 Atlantic Ocean. The dominant horizontal heat advections were through the P1 and P5, with the OFES2 showing

889 stronger heat advection at both the two passages. We calculated a downward heat diffusion at a depth of 2000 m of

890 0.216 W/m^2 in the OFES1 Atlantic Ocean and an upward VHD of 0.383 W/m^2 in the OFES2 Atlantic Ocean.

891   In the Indian Ocean, the calculated downward heat advection was two times stronger in the OFES1; there were

892   also some moderate differences in the horizontal heat advection. The resulting VHD at 2000 m was upward in both

893   the OFES1 and OFES2, but much greater (by 0.455 W/m^2) in the latter.

894   To summarize, differences in the lateral heat advection through the major passages P1–P10 in the lower layer was

895   small, and the major drivers of the examined OHC differences between the OFES1 and OFES2 came largely from the

896   vertical heat transport (VHA + VHD), similar to the situation in the middle layer.

897

898   **Table 4.** As for Tab. 2 but for the lower layer (700–2000 m). VHA is at a depth of 2000 m.

PACIFIC OCEAN (700–2000 m)								
	OHC	VHA	P3	P4	P5	P7	P8	P9	Residual
OFES1	0.058	−0.126	0.951	−0.047	−1.120	−0.035	0	0	−1.341
OFES2	−0.037	−0.105	1.146	−0.080	−1.294	−0.082	0	0	−0.089

ATLANTIC OCEAN (700–2000 m)						
	OHC	VHA	P1	P5	P6	P10	Residual
OFES1	0.014	−0.029	−0.974	1.120	0.066	0.105	−0.216
OFES2	−0.013	−0.536	−1.059	1.294	0.003	−0.031	0.383

INDIAN OCEAN (700–2000 m)						
	OHC	VHA	P1	P2	P3	P7	P8	Residual
OFES1	0.007	−0.241	0.974	−0.033	−0.951	0.035	0	0.126
OFES2	−0.018	−0.120	1.059	−0.052	−1.146	0.082	0	0.581

899   **4 Conclusions and Discussion**

900   In this paper, we estimated the OHC from two eddy-resolution hindcast simulations, OFES1 and OFES2, with a major

901   focus on their differences. The global observation-based dataset EN4 acted as a reference. The main findings were as

902   follows.

903   1. Multi-decadal warming was clearly seen in most of the global ocean (0–2000 m), especially in the EN4 and

904   OFES1. The warming was mainly manifested as deepening of the neutral density surfaces (HV component), with a

905   ~~lesser contribution from~~ changes along the neutral surfaces (SP component) of regional importance.

906   2. Significant differences in the OHC (or potential temperature) were found between the OFES1 and OFES2; the

907   major causes for these were fourfold. Firstly, there was generally more net surface heat flux in the OFES1. Secondly,

908   the ITF was almost two times stronger in the OFES2, especially in the top 300 m. Thirdly, the differences in the

909   intensity of the vertical heat advection were large, particularly at 300 m in the Indian Ocean. Finally, remarkable

910   differences in the vertical heat diffusion were inferred.

911   Although we have detailed the OHC differences between the OFES1 and OFES2, and also analysed the horizontal

912   and vertical heat transports in an attempt to understand the causes of these differences, more work is needed to

913   improve. Firstly, a direct calculation of the vertical heat diffusion was desirable to have a more reliable and accurate

914   comparison between the two datasets. In addition, decomposing the vertical heat diffusion into tidal mixing and mixed-

915   layer vertical mixing is also an interesting topic and may help to isolate the effects of tidal mixing on the ocean state.

916   Besides, we expect to see a detailed comparison of the wind stress from these two datasets over this 57-year period.

917   This is inspired by the work of Kutsuwada et al. (2019) and our detection of the large differences in the vertical heat

918   advection. Considering the apparent differences of the SP between the OFES2 and the other two datasets, a

919   comprehensive comparison of salinity between both the OFES1 and OFES2 with observations were required. This

920   helped the community to determine their choice of datasets for their own research purposes.

921   One may argue that being not well spun-up may be the major cause for the identified differences between the

922   OFES2 with others, since that the OFES1 followed a 50-year climatological simulation. This is likely to be a cause.

923   However, large differences between the two OFES datasets remain in the temporal evolution of the global and basin

924   OHCs, even during the last two decades. In addition, for example, **S2020** found that the Azores Current was simulated

925   in the OFES2 in the initial two decades but disappeared after 1970. This, to some extent, weaken the spin-up argument,

926   but does not rule out the possibility. The OFES2 was not expected to be highly sensitive to the spin-up issue, as it

927   started with conditions from the OFES1. That said, there were indeed some improvements in the OFES2 for the recent

928   decades, for example, over 2005-2016 (not shown here). Two potential explanations are: firstly, the model was full

929   spun-up after a couple of decades of integration; secondly, improvements of the reanalysis atmospheric forcing data

930   contributed to the simulation improvements.

931   One reviewer raised the concern on the uncertainty in the observational datasets (EN4) and suggested to add one

932   or two more observation-based datasets to reproduce some of our results here. We compared the temporal evolution

933   of OHC (Fig. S10) and spatial pattern of the long-term potential temperature trend (Fig. S11) between EN4 and two

934   more datasets, G10 and IAP. G10 is the most up to date version of EN4 datasets (EN4.2.2) with bias corrected

935   following Gouretski and Reseghetti (2010); and IAP is the dataset from the Institute of Atmospheric Physics (Cheng

936   and Zhu, 2016). The primary difference between the EN4 (bias corrected following Levitus et al. (2009)) and G10 is

937   the bias correction method, whereas IAP differs from EN4 in assimilated datasets, bias correction and mapping

938   methods. The high similarities between EN4 and G10 suggest that the different correction methods do not lead to

939   notable differences in the resulting state estimate. On the other hand, there do exist some differences between the IAP

940   and both EN4 and G10. This may indicate that mapping method applied cause some discrepancies among different

941   oceanic products, consistent with Cheng and Zhu (2016).

942   Finally, the OFES products, especially the OFES1, did capture some of the warming and cooling trends shown by

943   the EN4 and in the literature, despite their having no observational-based constraints. However, the clear differences

944   between the two OFES datasets and the EN4 suggest the importance of observational data in improving the hindcast

945   performance. The significant differences in the vertical heat diffusion between the two OFES datasets also suggest

946   that special attention should be given to validation of the vertical mixing scheme in future ocean modelling.

947

948   **Author contributions:** F.L conceived the study. All authors contributed to the details of study design. F.L conducted

949   the calculations and analysis. F.L drafted the manuscript; Z.L and X.H.W improved the writing.

Code and data availability: OFES1 and OFES2 are based on the MOM3, available at https://github.com/mom-ocean/MOM3. Code for decomposing the potential temperature: http://www.teos-10.org/software.htm. Original EN4 data: https://www.metoffice.gov.uk/hadobs/en4/download-en4-2-1.html. Original OFES1 temperature and salinity data: http://apdrc.soest.hawaii.edu/dods/public_ofes/OfES/ncep_0.1_global_mmean. Due to a data security incident, access to the OFES2 data has been temporarily suspended. The data and codes (including the publically available scripts for completion) needed to reproduce the results of this paper are archived on Zenodo (https://doi.org/10.5281/zenodo.5205444). The archived data are annual mean values calculated from the original data.

References

Abraham, J. P., Reseghetti, F., Baringer, M., Boyer, T., Cheng, L., Church, J., Domingues, C., Fasullo, J. T., Gilson, J., Goni, G., Good, S., Gorman, J. M., Gouretski, V., Ishii, M., Johnson, G. C., Kizu, S., Lyman, J., MacDonald, A., Minkowycz, W. J., Moffitt, S. E., Palmer, M., Piola, A., Trenberth, K. E., Velicogna, I., Wijffels, S., and Willis, J.: A review of global ocean temperature observations: implications for ocean heat content estimates and climate change, Rev. Geophys., 51, 450-483, doi.org/10.1002/rog.20022, 2013.

AchutaRao, K. M., Ishii, M., Santer, B. D., Gleckler, P. J., Taylor, K. E., Barnett, T. P., Pierce, D. W., Stouffer, R. J., and Wigley, T. M. L.: Simulated and observed variability in ocean temperature and heat content, Proc. Natl. Acad. Sci., 104,10768-10773, doi.org/10.1073/pnas.0611375104, 2007.

Allison, L. C., Roberts, C. D., Palmer, M. D., Hermanson, L., Killick, R. E., Rayner, N. A., Smith, D. M., and Andrews, M. B.: Towards quantifying uncertainty in ocean heat content changes using synthetic profiles, Environ. Res. Lett., 14, 084037, doi.org/10.1088/1748-9326/ab2b0b, 2019.

Balmaseda, M. A., Trenberth, K. E., and Källén, E.: Distinctive climate signals in reanalysis of global ocean heat content, Geophys. Res. Lett., 40, 1754-1759, doi.org/10.1002/grl.50382, 2013.

Bindoff, N. L., and McDougall, T. J.: Diagnosing climate change and ocean ventilation using hydrographic data, J. Phy. Oceanogr., 24, 1137-1152, doi.org/10.1175/1520-0485(1994)024<1137:DCCAOV>2.0.CO;2, 1994.

Carton, J. A., Chepurin,G. A. and Chen, L.: SODA3: A New Ocean Climate Reanalysis, *J. Climate.*, 31, 6967-6983, https://doi.org/10.1175/JCLI-D-18-0149.1, 2018.

Banks, H. T., and Gregory, J. M.: Mechanisms of ocean heat uptake in a coupled climate model and the implications for tracer based predictions of ocean heat uptake, Geophys. Res. Lett., 33, L07608, https://doi.org/10.1029/2005GL025352, 2006.

Carton, J. A., Chepurin, G., A. and Chen, L.: SODA3: A New Ocean Climate Reanalysis, J. Climate., 31, 6967-6983, https://doi.org/10.1175/JCLI-D-18-0149.1, 2018.

Carton, J. A., Penny, S. G., and Kalnay, E.: Temperature and salinity variability in the SODA3, ECCO4r3, and ORAS5 ocean reanalyses, 1993–2015, J. Climate., 32, 2277-2293, doi.org/10.1175/JCLI-D-18-0605.1, 2019.

Chen, X., Yan, Y., Cheng, X., and Qi, Y.: Performances of seven datasets in presenting the upper ocean heat content in the South China Sea, Adv. Atmos. Sci., 30, 1331-1342, doi.org/10.1007/s00376-013-2132-1, 2013.

Cheng, L., Trenberth, K. E., Palmer, M. D., Zhu, J., and Abraham, J.: Observed and simulated full-depth ocean heat content changes for 1970–2005, Ocean Sci., 12, 925-935, doi.org/10.5194/os-12-925-2016, 2016.

Cheng, L., and Zhu, J.: Artifacts in variations of ocean heat content induced by the observation system changes. Geophys. Res. Lett., 41, 7276-7283, https://doi.org/10.1002/2014GL061881, 2014.

Cheng, L., and Zhu, J.: Benefits of CMIP5 Multimodel Ensemble in Reconstructing Historical Ocean Subsurface Temperature Variations. J. Climate., 29(15), 5393–5416, https://doi.org/10.1175/JCLI-D-15-0730.1, 2016.

Cheng, L., Abraham, J., Goni, G., Boyer, T., Wijffels, S., Cowley, R., Gouretski, V., Reseghetti, F., Kizu, S., Dong, S., Bringas, F., Goes, M., Houpert, L., Sprintall, J., and Zhu, J.: XBT Science: Assessment of Instrumental Biases and Errors. Bull. Am. Meteorol. Soc., 97(6), 924–933, https://doi.org/10.1175/BAMS-D-15-00031.1, 2016.

Church, J. A., White, N. J., and Arblaster, J. M.: Significant decadal-scale impact of volcanic eruptions on sea level and ocean heat content, Nature, 438, 74-77, doi.org/10.1038/nature04237, 2005.

Curry, R., Dickson, B. and Yashayaev, I.: A change in the freshwater balance of the Atlantic Ocean over the past four decades. Nature, 426, 826-829, https://doi.org/10.1038/nature02206, 2003.

Desbruyères, D., McDonagh, E. L., King, B. A., and Thierry, V.: Global and Full-Depth Ocean Temperature Trends during the Early Twenty-First Century from Argo and Repeat Hydrography, J. Climate., 30, 1985-1997, doi.org/10.1175/JCLI-D-16-0396.1, 2017.

Desbruyeres, D., Purkey, S. G., Mcdonagh, E. L., Johnson, G. C. and King, B. A.: Deep and abyssal ocean warming from 35 years of repeat hydrography. Geophys. Res. Lett., 43, 10356-10365, doi.org/10.1002/2016GL070413, 2016.

1027
1028   Dong, S., Garzoli, S., and Baringer, M.: The role of interocean exchanges on decadal variations of the meridional heat

1029   transport in the South Atlantic, J. Phys. Oceanogr., 41, 1498-1511, doi.org/10.1175/2011JPO4549.1, 2011.

1030
1031   Durack, P. J., Gleckler, P. J., Landerer, F. W., and Taylor, K. E.: Quantifying underestimates of long-term upper-

1032   ocean warming, Nat. Climate Change., 4, 999-1005, https://doi.org/10.1038/nclimate2389, 2014.

1033
1034   Du, Y., Qu, T., Meyers, G., Masumoto, Y., and Sasaki, H.: Seasonal heat budget in the mixed layer of the southeastern

1035   tropical Indian Ocean in a high-resolution ocean general circulation model, J. Geophys. Res. Oceans., 110, C04012,

1036   doi.org/10.1029/2004JC002845, 2005.

1037
1038   Emery, W.: Water Types and Water Masses, Encyclopedia of Ocean Sciences, 4, 3179-3187,

1039   doi.org/10.1006/rwos.2001.0108, 2001.

1040
1041   Ernst, W. G.: *Earth systems: processes and issues.* Cambridge University Press, 2000.

1042
1043   Forget, G., Campin, J.-M., Heimbach, P., Hill, C. N., Ponte, R. M., and Wunsch, C.: ECCO version 4: an integrated

1044   framework for non-linear inverse modeling and global ocean state estimation, Geosci. Model Dev., 8 (10), 3071–

1045   3104, doi:10.5194/gmd-8-3071-2015, 2015.

1046
1047   Fyfe, J.: Southern Ocean warming due to human influence, Geophys. Res. Lett., 33, L19701, 10.1029/2006GL027247,

1048   2006.

1049
1050   Gleckler, P. J., Santer, B. D., Domingues, C. M., Pierce, D. W., Barnett, T. P., Church, J. A., Taylor, K. E., Achutarao,

1051   K., Boyer, T. P., and Ishii, M.: Human-induced global ocean warming on multidecadal timescales, Nat. Climate

1052   Change., 2, 524-529, doi.org/10.1038/nclimate1553, 2012.

1053
1054   Good, S. A., Martin, M., and Rayner, N. A.: EN4: Quality controlled ocean temperature and salinity profiles and

1055   monthly objective analyses with uncertainty estimates, J. Geophys. Res. Oceans., 118, 6704-6716,

1056   doi.org/10.1002/2013JC009067, 2013.

1057
1058   Gouretski, V., and Reseghetti, F.: On depth and temperature biases in bathythermograph data: Development of a new

1059   correction scheme based on analysis of a global ocean database. Deep Sea Res. Part I Oceanogr., 57(6), 812–833,

1060   https://doi.org/10.1016/j.dsr.2010.03.011, 2010.

1061
1062   Häkkinen, S., Rhines, P. B. and Worthen, D. L.: Heat content variability in the North Atlantic Ocean in ocean

1063   reanalyses, Geophys. Res. Lett., 42, doi.org/10.1002/2015GL063299, 2901-2909, 2015.

1064
1065   Häkkinen, S., Rhines, P. B., and Worthen, D.: Warming of the global ocean: Spatial structure and water-mass trends,

1066   J. Climate., 29, 4949-4963, doi.org/10.1175/JCLI-D-15-0607.1, 2016.

1067

IPCC.: Climate Change 2013: The Physical Science Basis. Cambridge University Press, 1535pp., doi:10.1017/CBO9781107415324, 2013.

Jackett, D. R., and McDougall, T. J.: A neutral density variable for the world's oceans, J. Phys. Oceanogr., 27, 237-263, doi.org/10.1175/1520-0485(1997)027<0237:ANDVFT>2.0.CO;2, 1997.

Jayne, S. R., and Laurent, L. C. St.: Parameterizing tidal dissipation over rough topography, Geophys. Res. Lett., 28, 811-814, doi.org/10.1029/2000GL012044, 2001.

Johnson, G. C., Purkey, S. G., Zilberman, N. V., and Roemmich, D. Deep Argo Quantifies Bottom Water Warming Rates in the Southwest Pacific Basin. Geophysical Research Letters, 46(5), 2662–2669, doi.org/10.1029/2018GL081685, 2019.

Kalnay, E., Kanamitsu, M., Kistler, R., Collins, W., Deaven, D., Gandin, L., Iredell, M., Saha, S., White, G., Woollen, J., Zhu, Y., Chelliah, M., Ebisuzaki, W., Higgins, W., Janowiak, J., Mo, K. C., Ropelewski, C., Wang, J., Leetmaa, A., Reynolds, R., Jenne, R., and Joseph, D.: The NCEP/NCAR 40-year reanalysis project, B. Am. Meteorol. Soc., 77, 437-472, doi.org/10.1175/1520-0477(1996)077<0437:TNYRP>2.0.CO;2, 1996.

Kutsuwada, K., Kakiuchi, A., Sasai, Y., Sasaki, H., Uehara, K., and Tajima, R.: Wind-driven North Pacific Tropical Gyre using high-resolution simulation outputs, J. Oceanogr., 75, 81-93, 10.1007/s10872-018-0487-8, 2019.

Large, W. G., McWilliams, J. C., and Doney, S. C.: Oceanic vertical mixing: A review and a model with a nonlocal boundary layer parameterization, Rev. Geophys., 32, 363-403, doi.org/10.1029/94RG01872, 1994.

Lee, S., Park, W., Baringer, M. O. A., Gordon, L., Huber, B. A., and Liu, Y.: Pacific origin of the abrupt increase in Indian Ocean heat content during the warming hiatus, Nature Geosci., 8, 445-449, doi.org/10.1038/ngeo2438, 2015.

Levitus, S., Antonov, J. I., Boyer, T. P., Baranova, O., Garcia, H. E., Locarnini, R. A., Mishonov, A. V., Reagan, J. R., Seidov, D., and Yarosh, E. S.: World ocean heat content and thermosteric sea level change (0–2000 m), Geophys. Res. Lett., 39, 1955-2010, doi.org/10.1029/2012GL051106, 2012.

Liang, X., Piecuch, C. G., Ponte, R. M., Forget, G., Wunsch, C., and Heimbach, P.: Change of the global ocean vertical heat transport over 1993–2010, J. Climate., 30, 5319-5327, doi.org/10.1175/JCLI-D-16-0569.1, 2017.

Liang, X., Liu, C. R., Ponte, M. and Chambers, D. P.: A Comparison of the Variability and Changes in Global Ocean Heat Content from Multiple Objective Analysis Products During the Argo Period, J. Climate., 1-47, doi.org/10.1175/JCLI-D-20-0794.1, 2021.

Liu, C., Liang, X., Chambers, D. P. and Ponte, R. M.: Global Patterns of Spatial and Temporal Variability in Salinity from Multiple Gridded Argo Products, J. Climate., 33, 8751-8766, https://doi.org/10.1175/JCLI-D-20-0053.1, 2020.

1108
1109 Liu, M., and T. Tanhua.: Water masses in the Atlantic Ocean: characteristics and distributions, Ocean Sci., 17, 463-
1110 486, doi.org/10.5194/os-17-463-2021, 2021.

1111
1112 Noh, Y., and Kim, H. J.: Simulations of temperature and turbulence structure of the oceanic boundary layer with the
1113 improved near-surface process, J. Geophys. Res. Oceans., 104, 15621-15634, doi.org/10.1029/1999JC900068, 1999.

1114
1115 O'Connor, B. M., Fine, R. A. and Olson, D. B.: A global comparison of subtropical underwater formation rates, Deep
1116 Sea Research Part I: Oceanographic Research Papers, 52, 1569-1590, doi.org/10.1016/J.DSR.2005.01.011, 2005.

1117
1118 Palmer, M. D., Mcneall, D. J., and Dunstone, N. J.: Importance of the deep ocean for estimating decadal changes in
1119 Earth's radiation balance, Geophys. Res. Lett., 38, L13707, doi.org/10.1029/2011GL047835, 2011.

1120
1121 Pierce, D. W., Barnett, T. P., Achutarao, K., Gleckler, P. J., Gregory, J. M., and Washington, W. M.: Anthropogenic
1122 warming of the oceans: Observations and model results, J. Climate., 19, 1873-1900, doi.org/10.1175/JCLI3723.1,
1123 2006.

1124
1125 Sasaki, H., Sasai, Y., Kawahara, S., Furuichi, M., Araki, F., Ishida, A., Yamanaka, Y., Masumoto, Y., and Sakuma,
1126 H.: A series of eddy-resolving ocean simulations in the world ocean-OFES (OGCM for the Earth Simulator) project,
1127 Oceans '04 MTS/IEEE Techno-Ocean '04 (IEEE Cat. No. 04CH37600) 3, 1535-1541, 2004.

1128
1129 Sasaki, H., Kida, S., Furue, R., Aiki, H., Komori, N., Masumoto, Y., Miyama, T., Nonaka, M., Sasai, Y., and Taguchi,
1130 B.: A global eddying hindcast ocean simulation with OFES2, Geosci. Model Dev., 13, 3319-3336,
1131 doi.org/10.5194/gmd-13-3319-2020, 2020.

1132
1133 Smith, D. M., Allan, R.P., Coward, A.C., Eade, R., Hyder, P., Liu, C., Loeb, N.G., Palmer, M.D., Roberts, C.D. and
1134 Scaife, A.A.: Earth's energy imbalance since 1960 in observations and CMIP5 models, Geophys. Res. Lett., 42, 1205-
1135 1213, doi.org/10.1002/2014GL062669, 2015.

1136
1137 Spence, P., Saenko,O. A., Sijp, W., and England, M.: The role of bottom pressure torques on the interior pathways of
1138 North Atlantic deep water, J. Phys. Oceanogr., 42, 110-125, doi.org/10.1175/2011JPO4584.1, 2012.

1139
1140 St. Laurent, L. C., Simmons, H. L., and Jayne, S. R.: Estimating tidally driven mixing in the deep ocean, Geophys.
1141 Res. Lett., 29, 21-21–21-24, doi.org/10.1029/2002GL015633, 2002.

1142
1143 Talley, L. D.: Shallow, Intermediate, and Deep Overturning Components of the Global Heat Budget, J. Phys.
1144 Oceanogr., 33, 530-560, https://doi.org/10.1175/1520-0485(2003)033<0530:SIADOC>2.0.CO;2, 2003.

1145
1146 Trenberth, K. E., Fasullo, J. T., Von Schuckmann, K., and Cheng, L.: Insights into Earth's energy imbalance from
1147 multiple sources, J. Climate., 29, 7495-7505, doi.org/10.1175/JCLI-D-16-0339.1, 2016.

1148

1149 Tsujino, H., Urakawa, S., Nakano, H., Small, R. J., Kim, W. M., Yeager, S. G., Danabasoglu, G., Suzuki, T., Bamber,
1150 J. L., Bentsen, M., Böning, C. W., Bozec, A., Chassignet, E. P., Curchitser, E., Boeira Dias, F., Durack, P. J., Griffies,
1151 S. M., Harada, Y., Ilicak, M., Josey, S. A., Kobayashi, C., Kobayashi, S., Komuro, Y., Large, W. G., Le Sommer, J.,
1152 Marsland, S. J., Masina, S., Scheinert, M., Tomita, H., Valdivieso, M., and Yamazaki, D.: JRA-55 based surface
1153 dataset for driving ocean-sea-ice models (JRA55-do), Ocean Model., 130, 79-139,
1154 doi.org/10.1016/j.ocemod.2018.07.002, 2018.

1156 Von Schuckmann, K., Palmer, M. D., Trenberth, K. E., Cazenave, A., Chambers, D. P., Champollion, N., Hansen, J.,
1157 Josey, S. A., Loeb, N. G., and Mathieu, P. P.: An imperative to monitor Earth's energy imbalance, Nat. Climate
1158 Change., 6, 138-144, doi.org/10.1038/nclimate2876, 2016.

1160 Wang, G., Cheng, L., Abraham, J., and Li, C.: Consensuses and discrepancies of basin-scale ocean heat content
1161 changes in different ocean analyses, Clim. Dyn., 50, 2471-2487, doi.org/10.1007/s00382-017-3751-5, 2018.

1163 Wang, X. H., Bhatt, V., and Sun, Y.-J.: Study of seasonal variability and heat budget of the East Australian Current
1164 using two eddy-resolving ocean circulation models, Ocean. Dyn., 63, 549-563, doi.org/10.1007/s10236-013-0605-5,
1165 2013.

1167 Wunsch, C.: The decadal mean ocean circulation and Sverdrup balance, J. Mar. Res., 69, 417-434, doi.org/
1168 10.1357/002224011798765303, 2011.

1170 Zanna, L., Khatiwala, S., Gregory, J. M., Ison, J., and Heimbach, P.: Global reconstruction of historical ocean heat
1171 storage and transport, Proc. Natl. Acad. Sci., 116, 1126-1131, doi.org/10.1073/pnas.1808838115, 2019.

1173 Zhang, Y., Feng, M., Du,Y. H., Phillips, E., Bindoff, N. L., and McPhaden, M. J.: Strengthened Indonesian
1174 Throughflow Drives Decadal Warming in the Southern Indian Ocean, Geophys. Res. Lett., 45, 6167-6175,
1175 doi.org/10.1029/2018GL078265, 2018.

1176
1177
1178
1179
1180